Dalitz Analysis of $B^- \to D^+\pi^-\pi^-$

Master Thesis

Author: Bhavesh Sirvi (Student ID: 411037)
Supervisor: Prof. Dr. Jan Jolie
Co-Supervisor: Prof. Dr. Florian Bernlochner

Department of Physics
Faculty of Mathematics and Natural Sciences
University of Cologne

November 6, 2024

Eidesstattliche Versicherung

Hiermit versichere ich an Eides statt, dass ich die vorliegende Arbeit selbstständig und ohne die Benutzung anderer als der angegebenen Hilfsmittel angefertigt habe. Alle Stellen, die wörtlich oder sinngemäß aus veröffentlichten und nicht veröffentlichten Schriften entnommen wurden, sind als solche kenntlich gemacht. Die Arbeit ist in gleicher oder ähnlicher Form oder auszugsweise im Rahmen einer anderen Prüfung noch nicht vorgelegt worden. Ich versichere, dass die eingereichte elektronische Fassung der eingereichten Druckfassung vollständig entspricht.

Die Strafbarkeit einer falschen eidesstattlichen Versicherung ist mir bekannt, namentlich die Strafandrohung gemäß § 156 StGB bis zu drei Jahren Freiheitsstrafe oder Geldstrafe bei vorsätzlicher Begehung der Tat bzw. gemäß § 161 Abs. 1 StGB bis zu einem Jahr Freiheitsstrafe oder Geldstrafe bei fahrlässiger Begehung.

Bhavesh Sirvi

Köln, den 06.11.2024

Abstract

Fully hadronic B meson decays provide a powerful tool for studying the hadronic properties of excited D meson states beyond the 1S ground state, which remain not well-explored. This thesis presents the study of the decay $B^- \to D^+\pi^-\pi^-$, aimed at investigating orbitally excited 1P charm states. The goal of this work is to determine their widths, masses, spin, and other key properties.

A Dalitz analysis is carried out by reconstructing the decay $B^- \to D^+\pi^-\pi^-$ via $D^+ \to K^-\pi^+\pi^+$ decays. Simulated Belle II data are analyzed to show the sensitivity of the analysis to physical parameters, assuming the integrated luminosity of Run 1. Gaining a more precise understanding of these charm states will aid in improving our knowledge of semileptonic processes, such as $B^+ \to D^*\tau^+\nu_\tau$, where semileptonic contributions from higher charm states are an important background. This improved understanding will help reduce uncertainties in future determinations of the elements of the Cabibbo-Kobayashi-Maskawa (CKM) matrix.

Contents

List of Figures

List of Tables

1 Introduction

The Standard Model (SM) successfully unifies electromagnetism, the weak force, and the strong force, providing a highly accurate description of nature. It has been extensively validated through numerous experiments and continues to be tested with modern detectors. Despite its remarkable success, some parameters are yet to be measured precisely, such as the matrix element $|V_{cb}|$ of the Cabibbo-Kobayashi-Maskawa (CKM) matrix, which is critical for testing the unitarity of the CKM matrix. Semi-leptonic decays provide the best precision measurements of $|V_{cb}|$, as they occur at tree level in the lowest order of the SM and are unaffected by physics beyond the SM [6]. While the decay $B^+ \to D^*\ell^+\nu_\ell$ is an excellent candidate for determining $|V_{cb}|$, achieving precise measurements also requires a better understanding of the background from D^{**} states, which are orbitally excited states of the D meson [7].

To investigate these states in detail, we will reconstruct the decay channel $B^- \to D^+\pi^-\pi^-$ [1] using the simulated data corresponding to Belle II's Run 1 integrated luminosity . This decay is anticipated to include contributions from D^{**} states. The channel has previously been analyzed by several experiments such as LHCb [8], Belle II [1] and BaBar [7] using the Dalitz plot technique, which reveals resonant states through characteristic structures associated with the different angular momenta of the D-meson excitations. Studying these states in detail will help reduce uncertainties associated with measurements of semileptonic decays, thereby improving the determination of the Cabibbo-Kobayashi-Maskawa matrix elements $|V_{cb}|$ and $|V_{ub}|$ and can also serves as a test for Heavy Quark Effective Theory [7].

D_J Excited D Mesons

The D^{**} states, represented as D_J, are the P-wave excitations (where $J = 1$) of quark-antiquark systems composed of one charm and one light quark. The P-wave D-meson states include two $j = 1/2$ states and two $j = 3/2$ states, resulting in four states with specific spin-parity J^P assignments as show in Fig 1:

- $j = 1/2$ states:
  - $J^P = 0^+$, referred to as D_0^{*0},
  - $J^P = 1^+$, referred to as $D_1'(2430)^0$,
- $j = 3/2$ states:
  - $J^P = 1^+$, referred to as $D_1(2420)^0$,
  - $J^P = 2^+$, referred to as D_2^{*0}.

[1] The charged conjugated modes are implied throughout the text unless specified otherwise.

Resonance	J^P	Mass (MeV/c^2)	Width (MeV/c^2)	Partial Wave
D_0^{*0}	2^+	2461.1 ± 0.7	47.3 ± 0.8	D
	0^+	2343 ± 10	229 ± 16	S
D_2^{*0}	2^+	2461.1 ± 0.7	47.3 ± 0.8	D

Table 1: Expected P-wave resonances [5].

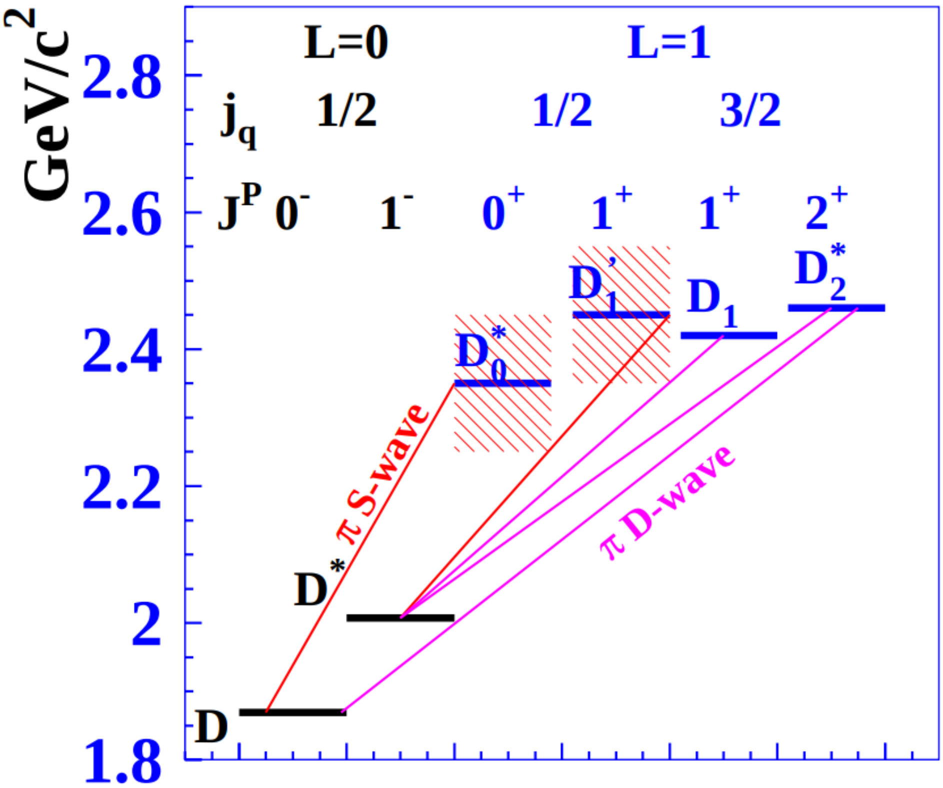

Figure 1: D_J mass spectrum. The red dashed bins shows the width and the lines show the allowed transitions [1].

Since this analysis reconstructs charged D mesons ($J = 0$) combined with two pions in the final state, only contributions from neutral resonances are expected:

- $j = 1/2$: D_0^{*0} (a broad S-wave resonance),
- $j = 3/2$: D_2^{*0} (a narrower D-wave resonance).

The D_0^{*0} decays to $D\pi$, while the D_2^{*0} decays to both $D\pi$ and $D^*\pi$, as shown in Fig 2.

A key challenge in modeling decays involves handling broad resonances is that they interfere with nonresonant amplitudes within the same partial wave [8]. In the decay $B^- \to D^+\pi^-\pi^-$, this issue is especially significant in the $D^+\pi^-$ S-wave, where the $D_0^*(2400)^0$ resonance coexists with a nonresonant component. For the $D_0^*(2400)^0$ resonance, a fitting technique using splines describes both the magnitude and phase as functions of the Dalitz plot variable which enables the calculation of the total amplitude. LHCb has extended this approach to the entire $D^+\pi^-$ S-wave, encompassing both

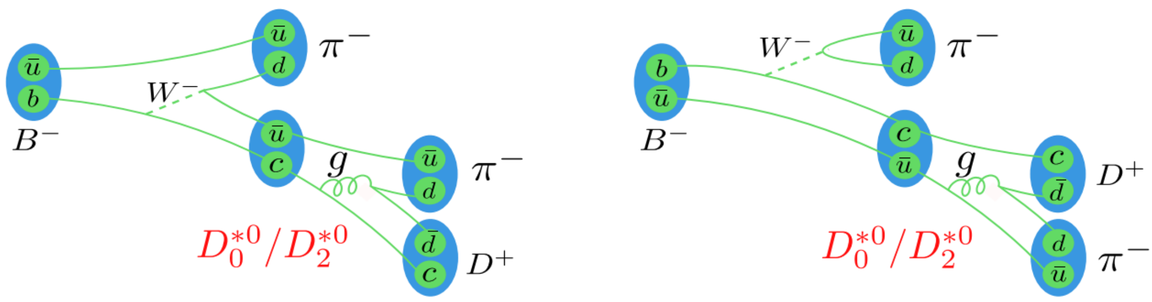

Figure 2: Tree-level Feynman diagrams for the scalar and tensor resonance.

the $D_0^*(2400)^0$ resonance and the nonresonant component. This approach would have been better but the limitation was statistics, instead the resonances were modelled with Relativisitic Breit Wigner lineshape.

In this analysis, we use Monte Carlo (MC) data, detailed in Chapter 4, generated with `EVTGEN`, which does not account for interference effects. Nevertheless, this analysis will serve as a foundation for later applications to the complete Belle II dataset.

Structure of the Thesis

Chapter 2 provides a brief description of the Belle II experiment. Chapter 3 details the analysis techniques employed in this study, including the Dalitz plot formalism and the fitting framework LAURA^{++}. Chapter 4 describes the simulated samples used in this analysis, along with the reconstruction and selection of the entire decay chain. Chapter 5 discusses the background subtraction technique using sPlot. Chapter 6 explains the detector efficiency in detail, while Chapter 7 outlines the fit model. Chapter 8 presents the fit validation, and Chapter 10 includes the fit results and discussion.

2 The BELLE II experiment

SuperKEKB

SuperKEKB, constructed by upgrading the KEK B-Factory, is an asymmetric-energy electron–positron double-ring collider. It collides electrons (e^-) and positrons (e^+) with energies of 7 GeV in the high-energy ring (HER) and 4 GeV in the low-energy ring (LER), respectively as depicted in the Fig 3. In 2022, SuperKEKB set a new world record for luminosity, achieving $4.7 \times 10^{34}\,\mathrm{cm}^{-2}\,\mathrm{s}^{-1}$ using the nano-beam scheme [9].

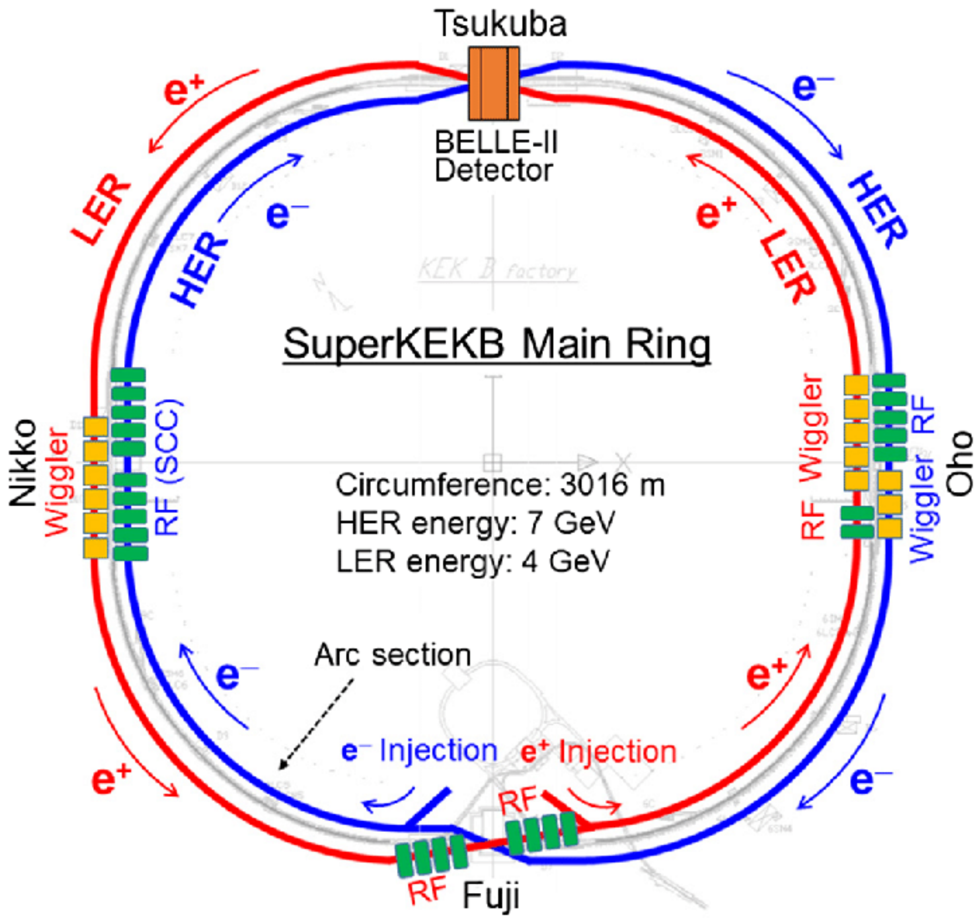

Figure 3: Layout of the SuperKEKB collider [2]

The e^+e^- system collides at the interaction point inside the Belle II detector with a center of mass (COM) energy, $\sqrt{s}$, of 10.58 GeV, corresponding to the resonance mass of the $\Upsilon(4S)$ meson—an excited state of the $b\bar{b}$ system, just above the $B\bar{B}$ production threshold. The $\Upsilon(4S)$ meson promptly decays almost 100% into an entangled pair of $B\bar{B}$ mesons without producing any additional particles [10]. In the COM frame, the produced B mesons are nearly at rest. Due to the short lifetime of B mesons (about 10^{-12} s), the forward Lorentz boost from the asymmetric beam energies allows the B mesons to travel some distance within the detector before decaying, enabling precise measurements of their lifetimes, mixing parameters, and CP violation.

By adjusting the COM energy, SuperKEKB can also operate just below or above the $\Upsilon(4S)$ resonance, suppressing $B\bar{B}$ production and allowing the study of continuum backgrounds, which are important for understanding background contributions in other analyses.

The BELLE II detector

At the interaction point of the SuperKEKB is the BELLE II detector. The Belle II detector is a full solid angle detector with dimensions of 8×8 meters, and it is equipped with multiple sub-detector layers surrounding the interaction point. Replacing the old Belle detector, Belle II aims to achieve high performance in a significantly higher background environment (10-20 times) due to the increased luminosity (40 times) of the SuperKEKB collider [11].

The detector is composed of several sub-detectors, including the Vertex Detector (VXD), the Central Drift Chamber (CDC), Particle Identification (PID) systems, the Electromagnetic Calorimeter (ECL), and the KLong and Muon detector (KLM) [12, 13]. Figure 4 shows a cross-sectional view of the Belle II detector.

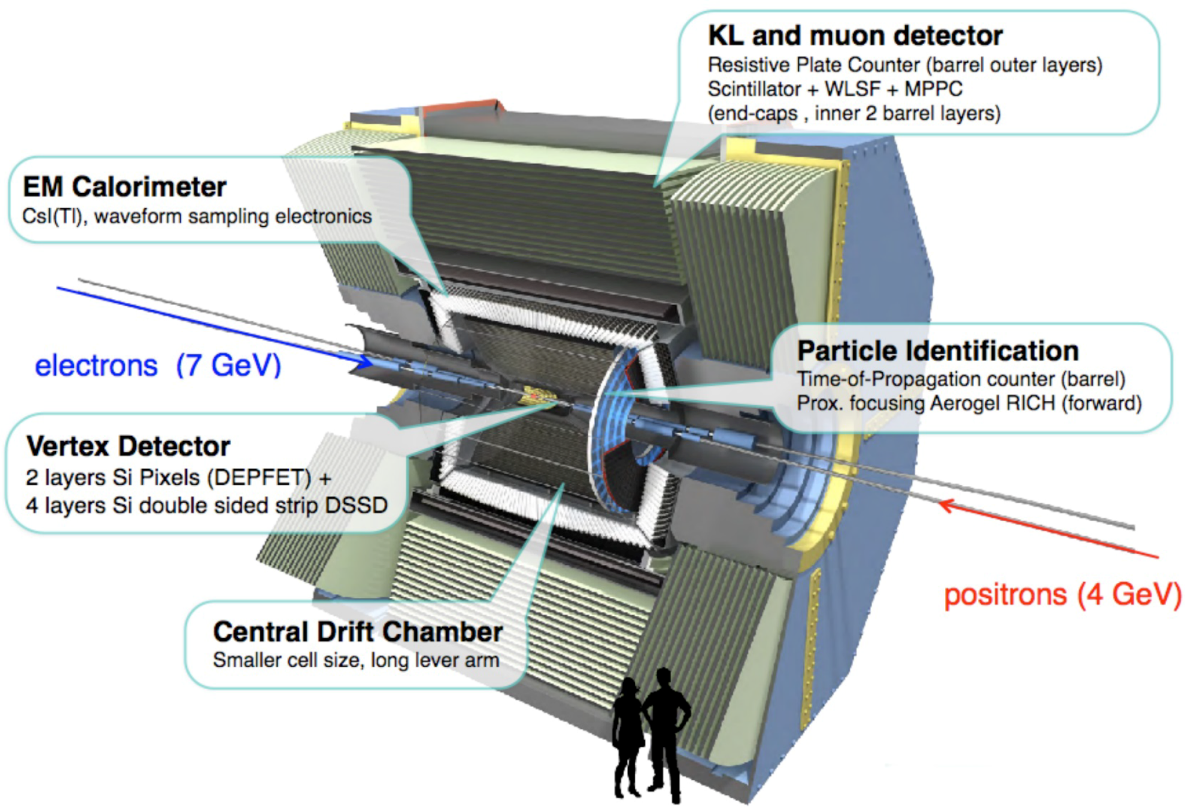

Figure 4: Cross section of the BELLE II detector with all the sub-detectors. [3]

VXD

VXD consists of two sub-detectors: the Pixel Detector (PXD) and the Silicon Vertex Detector (SVD). The PXD comprises two layers of DEPFET (Depleted p-channel Field Effect Transistor) technology. These layers are crucial for precise vertex reconstruction and are designed to handle the high hit rates near the beam pipe. The SVD, made up of four layers of double-sided silicon strip detectors (DSSD), extends outward from the PXD. This system provides excellent timing resolution, complementing the high spatial resolution of the PXD. Together, the PXD and SVD allow the detector to track low-momentum particles with high efficiency and accurately measure decay vertices for B mesons, D mesons, and τ leptons [13].

CDC

The CDC is filled with a mixture of 50% He and 50% C_2H_6 and consists 14336 sense wires arranged in 56 layers [12]. CDC reconstructs charged particle tracks determine their momenta accurately. The energy loss $\frac{dE}{dx}$ in its gas volume provides information for particle identification. Additionally, it also generates trigger information for charged particles.

PID

Belle II features two new PID systems: the Time of Propagation (TOP) detector and the Aerogel Ring Imaging Cherenkov (ARICH) detector. The TOP detector is located in the barrel region and is designed to improve separation of kaons from pions by measuring the time of flight and the Cherenkov angle of detected particles. The ARICH detector is located in the forward end-cap and uses two layers of aerogel with different refractive indices to generate Cherenkov light. This allows for precise separation of kaons from pions across a wide momentum range.

ECL

The Electromagnetic Calorimeter (ECL) is composed of thallium-doped cesium iodide (CsI(Tl)) crystals in the barrel region and pure CsI crystals in the end-caps. Its primary function is to measure electromagnetic energy and identify photons and electrons produced during collisions. The interactions vary depending on the type and momentum of the incoming particle; however, the electromagnetic energy deposited is measured by analyzing the intensity of the emitted scintillation photons.

KLM

KLM is composed of alternating layers of iron plates and resistive plate chambers (RPCs) in the barrel region, and scintillators in the end-cap regions. The KLM is designed to detect and identify between muons and K_L^0 mesons. While K_L^0 mesons undergo hadronic showers either in the KLM or the ECL, muons penetrate deeper into the KLM, allowing for their identification. The penetration of muons depends on their momentum and the energy they deposit. Muons with momentum greater than 1.5 GeV can traverse the entire detector, while those with momentum less than 0.7 GeV are unable to reach the KLM. [14].

3 Analysis techniques

3.1 Dalitz plot analysis formalism

3.1.1 Dalitz Plot

The Dalitz plot analysis technique, developed by Richard Dalitz during his study of the tau-theta puzzle, enables the examination of three-body decays with intermediate resonances based on their kinematics. Unlike two-body decays, three-body decays have additional intrinsic degrees of freedom, allowing the determination of both the relative magnitudes and phases of interfering amplitudes.

A three-body decay has 12 degrees of freedom. Conservation of momentum imposes 3 constraints, energy conservation imposes an additional constraint, the fixed masses of the final-state particles impose 3 further constraints, bringing the total to 5.

For decays where both the initial and final-state particles are spinless, the overall spatial orientation of the system becomes irrelevant. This rotational symmetry imposes 3 additional constraints, as the decay configuration can be aligned into a fixed reference frame using Euler angles [15]. As a result, for spin-0 decays, the phase space can be fully described by just two variables. The scatter plot of this pair of variables is known as the DP, which provides a complete representation of the decay kinematics.

There is flexibility in choosing which two variables to describe the amplitude of the decay. A common choice involves using the kinetic energies of two of the final-state particles or, alternatively, the squares of the invariant masses of two pairs of final-state particles (e.g., m_{23}^2 and m_{13}^2). In this analysis, we adopt the latter approach, which is particularly suited for relativistic decays.

For a particle of mass M decaying into three particles labeled a, b, and c, the differential decay probability is expressed as:

$$d\Gamma = \frac{1}{(2\pi)^3} \frac{|A|^2}{32M^3} \, dm_{ab}^2 \, dm_{bc}^2 \tag{1}$$

where m_{ab} and m_{bc} are the invariant masses of the particle pairs ab and bc, respectively. The prefactor includes all kinematic factors, while $|A|^2$ characterizes the dynamics of the process. For non-resonant decays, the decay amplitude A is independent of m_{ab}^2 and m_{bc}^2, resulting in a uniform population of events across the DP. Any structure or variation observed in the DP is attributed to resonant decays, allowing for detailed analysis of the underlying decay dynamics. Figure 5 shows examples of different structures possible due to spin and interference.

Further details on the DP analysis technique can be found in the respective chapters of The Physics of B Factories and LAURA^{++}:A Dalitz plot fitter [4, 16].

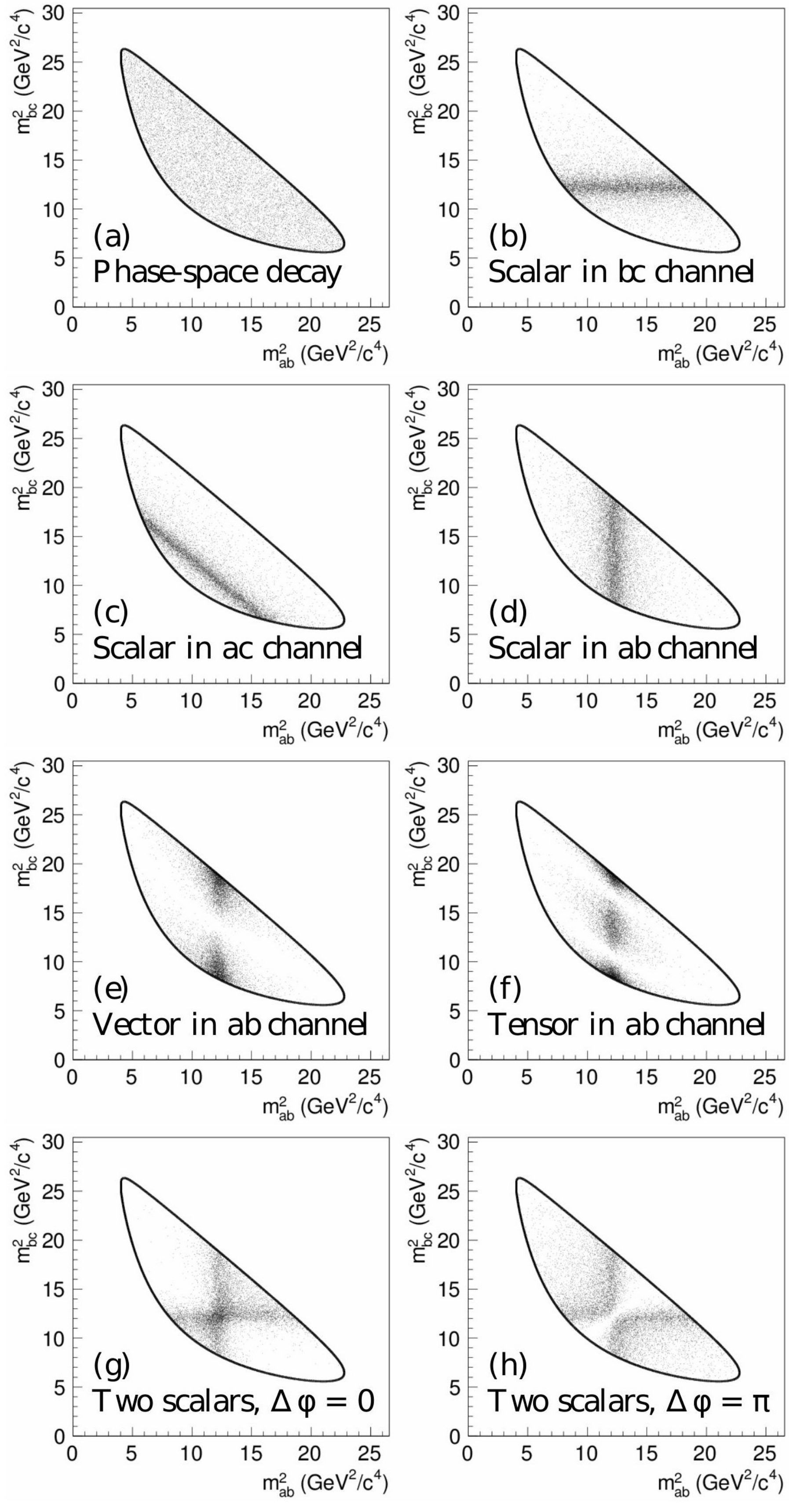

Figure 5: Dalitz plots showing (a) phase-space decay, (b-d) a scalar resonance manifesting in different decay channels, (e, f) vector and tensor resonances, and (g, h) the interference between two scalar resonances with varying values of the relative phase $\Delta\phi$. [4]

3.1.2 Kinematic Boundaries

The invariant masses of pairs of final-state particles are constrained by the following relationship:

$$m_{ab}^2 + m_{bc}^2 + m_{ac}^2 = M^2 + m_a^2 + m_b^2 + m_c^2, \tag{2}$$

where M is the total mass of the decaying particle and m_a, m_b, and m_c are the masses of the final-state particles. The right-hand side remains constant for a given decay, indicating that all relevant kinematic information is encapsulated in two of the invariant mass combinations. This leads to three possible definitions of the DP: (m_{ab}^2, m_{bc}^2), (m_{ac}^2, m_{bc}^2), and (m_{ab}^2, m_{ac}^2).

The maximum value of a specific invariant mass is reached when the third final-state particle is produced at rest in the decaying particle's rest frame. For a given value of one invariant mass, such as m_{ab}^2, the range of the other invariant masses can be expressed as:

$$(m_{bc}^2)_{\max} = (E_b^* + E_c^*)^2 - (p_b^* - p_c^*)^2, \tag{3}$$

$$(m_{bc}^2)_{\min} = (E_b^* + E_c^*)^2 - (p_b^* + p_c^*)^2, \tag{4}$$

where E_b^* and E_c^* are the energies of particles b and c in the rest frame of the ab-system, and are given by:

$$E_b^* = \frac{m_{ab}^2 - m_a^2 + m_b^2}{2m_{ab}}, \quad E_c^* = \frac{M^2 - m_{ab}^2 - m_c^2}{2m_{ab}}. \tag{5}$$

The corresponding momenta p_b^* and p_c^* are:

$$p_b^* = \sqrt{E_b^{*2} - m_b^2}, \quad p_c^* = \sqrt{E_c^{*2} - m_c^2}. \tag{6}$$

This defines the kinematically allowed region in the DP, where the boundary points correspond to configurations in which the final-state particles are collinear. At these extreme points, one of the invariant masses reaches its maximum value when the third particle is at rest, and the remaining two particles have back-to-back momenta. Conversely, the minimum value occurs when the third particle carries the maximum possible momentum. An example of different kinematic configurations on the DP, which illustrates the regions corresponding to the allowed phase space of a three-body decay, is shown in Figure 6.

3.1.3 Amplitude Description

In the context of nonleptonic three-body decays, B and D mesons primarily decay through resonant two-body processes. The decay amplitude $A(m_{ab}^2, m_{bc}^2)$ is typically modeled as

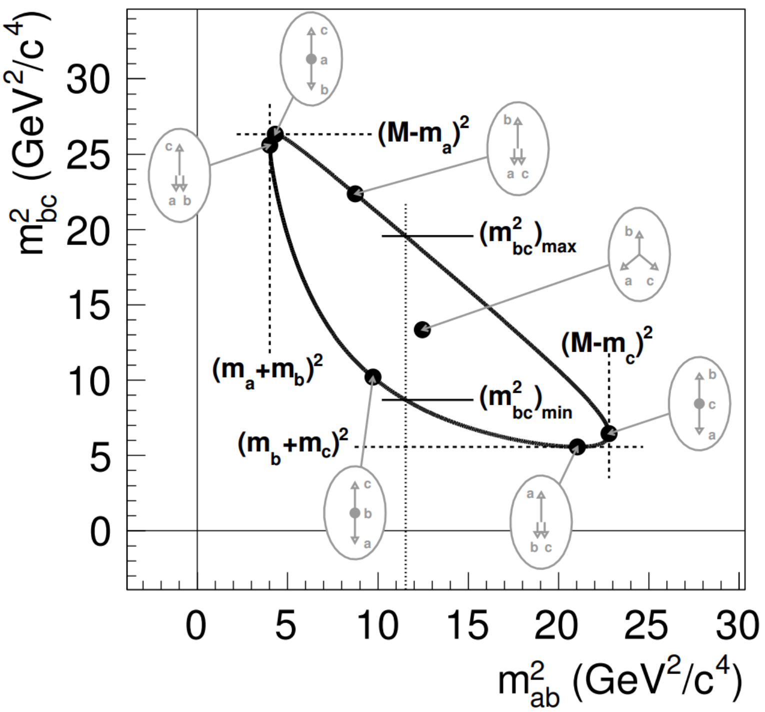

Figure 6: The kinematic boundaries and various possible configurations in a three-body decay are represented in a Dalitz plot.

a coherent sum of resonant two-body amplitudes along with a nonresonant contribution. This relationship is mathematically expressed as:

$$A(m) = \sum_r a_r e^{i\phi_r} A_r(m) + a_{NR} e^{i\phi_{NR}} A_{NR}(m). \tag{7}$$

In this equation, a_r represents the magnitude of the amplitude for each resonant component r, while a_{NR} denotes the magnitude of the nonresonant contribution. The phases ϕ_r and ϕ_{NR} correspond to these respective contributions. The functions A_r and A_{NR} are Lorentz-invariant expressions that encode the dynamical properties of the decay into the multi-body final state as a function of the positions in the DP, denoted as $m \equiv (m^2_{ab}, m^2_{bc})$.

3.1.3.1 Isobar Formalism A_r can be parameterized in the isobar formalism [17] where each function A_r describes a single intermediate resonance and the total amplitude is described as a coherent sum of N amplitudes from resonant or non-resonant intermediate processes.

$$A(m^2_{ab}, m^2_{bc}) = \sum_{j=1}^{N} c_j A_j(m^2_{ab}, m^2_{bc}) \tag{8}$$

A_r can be written as:

$$A_r = F_P \times F_r \times T_r \times W_r, \tag{9}$$

where F_P and F_r are the transition form factors of the parent particle and resonance, respectively. They are also called as angular momentum barrier factor. The resonance propagator $T_r \times W_r$ describes the line shape (T_r) and angular dependence (W_r) of the resonance.

3.1.3.2 Angular Distributions and Blatt–Weisskopf Form Factors The angular dependence $W_r = W(\vec{p}, \vec{q})$ is determined using the Zemach tensor formalism [18, 19]. These distributions are expressed as follows for different values of the orbital angular momentum L:

$$L = 0: \quad W(\vec{p}, \vec{q}) = 1, \tag{10}$$
$$L = 1: \quad W(\vec{p}, \vec{q}) = -2\,\vec{p} \cdot \vec{q}, \tag{11}$$
$$L = 2: \quad W(\vec{p}, \vec{q}) = \frac{4}{3}\left[3(\vec{p} \cdot \vec{q})^2 - (|\vec{p}| \cdot |\vec{q}|)^2\right], \tag{12}$$

where $\vec{p}$ is the momentum of one of the resonance daughters, and $\vec{q}$ is the momentum of the bachelor particle, both evaluated in the rest frame of the resonance. The term $\vec{p} \cdot \vec{q}$ is proportional to $\cos(\theta_H)$, where θ_H is the helicity angle defined as the angle between $\vec{p}$ and $\vec{q}$. The helicity angle θ_H describes angular distributions in decays. It can be calculated as follows: θ_{ij} is defined as the angle between decay products d_i and d_j in the rest frame of the d_i and d_j system, where $\vec{q}$ is the momentum of d_i. As a result, the angular distribution also reveals information about the spin of the resonance, leading to bands appearing in the DP: a spin-0 resonance has a flat distribution, a spin-1 resonance follows $\cos^2\theta_{ij}$, and a tensor resonance follows $|3\cos^2\theta_{ij} - 1|^2$.

These expressions are multiplied by a factor of $(-2pq)^L$, which serves as an angular momentum barrier, suppressing the amplitude at low values of the break-up momentum for either the parent or resonance decay [16]. Without additional modifications, the amplitude would continue to increase as the break-up momentum grows, even after surpassing the barrier. The terms F_P and F_r are described using the Blatt–Weisskopf parametrization form factors [20], which control this growth by limiting the amplitude beyond the barrier. These form factors are given by:

$$J = 0: \quad F = 1, \tag{13}$$
$$J = 1: \quad F = \sqrt{\frac{1 + R^2 q_r^2}{1 + R^2 q_{ab}^2}}, \tag{14}$$
$$J = 2: \quad F = \sqrt{\frac{9 + 3R^2 q_r^2 + R^4 q_r^4}{9 + 3R^2 q_{ab}^2 + R^4 q_{ab}^4}}. \tag{15}$$

Here, R is the meson radius, which usually takes values between 1 and 5 GeV^{-1}. This analysis will use a value of $R = 4\,\mathrm{GeV}^{-1}$.

3.1.3.3 Line Shapes The line shapes are used for the dynamical function T_r to parametrize resonance shapes, Relativistic Breit-Wigner (RelBW) is the most common line shape with a mass-dependent width Γ_{ab}

$$T_r = \frac{1}{(m_r^2 - m_{ab}^2) - i m_r \Gamma_{ab}}, \tag{16}$$

where m_r is the nominal mass of the resonance. The dependence of the decay width of the resonance on m is given by:

$$\Gamma_{ab} = \Gamma_r \left(\frac{q_{ab}}{q_r}\right)^{2J+1} \left(\frac{m_r}{m_{ab}}\right) F_r^2, \tag{17}$$

where Γ_r and J are the width and spin of the resonance, q_{ab} is the momentum of the daughter particles in the center-of-mass frame of particles a and b, and q_r is the momentum the decay products would have in the rest frame of a resonance with mass m_r. L represents the orbital angular momentum between the resonance daughters. Since all initial- and final-state particles have zero spin, L corresponds to both the spin of the resonance and the orbital angular momentum between the resonance and the bachelor particle. The Breit-Wigner parameterization works well only in the case of narrow states

3.1.4 Fit Fractions

Differences in normalization, phase conventions, and amplitude formalisms across experiments and fitting packages makes the comparison of complex coefficients between analyses difficult [4, 8]. Fit fractions serve as a tool for such comparisons and help estimate the branching fractions of different decay modes. The fit fraction for the jth channel is defined as the integral of a single decay amplitude squared, divided by the integral of the coherent matrix element squared for the complete DP:

$$FF_j = \frac{\int\int_{\mathrm{DP}} |c_j A_j(m_{13}^2, m_{23}^2)|^2 \, dm_{13}^2 \, dm_{23}^2}{\int\int_{\mathrm{DP}} |A(m_{13}^2, m_{23}^2)|^2 \, dm_{13}^2 \, dm_{23}^2}, \tag{18}$$

where c_j are the complex coefficients in the isobar model, as given in Equation 8, which represent the relative contributions of each intermediate process and are calculated by fitting to the data. These coefficients can be expressed as:

$$c_j = |c_j| e^{i\phi_j}, \tag{19}$$

or alternatively, using the real and imaginary parts:

$$c_j = x_j + iy_j. \tag{20}$$

The sum of fit fractions need not equal unity due to interference effects, which can be captured by:

$$FF_{ij} = \frac{\int\int_{\mathrm{DP}} 2\mathrm{Re}(c_i c_j^* F_i F_j^*)\, dm_{13}^2\, dm_{23}^2}{\int\int_{\mathrm{DP}} |A|^2\, dm_{13}^2\, dm_{23}^2}. \tag{23}$$

3.1.5 Symmetric Dalitz Plot

In three-body decay modes involving two identical final-state particles, such as the decay $B^- \to D^+\pi_1^-\pi_2^-$, the DP exhibits a symmetry along the diagonal where $m^2(D^+\pi_1^-) = m^2(D^+\pi_2^-)$. By exploiting this symmetry, the DP can be "folded," effectively increasing the available statistics [8].

Instead of using the invariant mass combinations $m^2(D^+\pi_1^-)$ and $m^2(D^+\pi_2^-)$, we introduce the following redefinitions of the kinematic variables:

- **Maximal invariant mass pair:**

$$m^2(D^+\pi^-)_{\mathrm{max}} = \begin{cases} m^2(D^+\pi_1^-), & \text{if } m^2(D^+\pi_1^-) > m^2(D^+\pi_2^-) \\ m^2(D^+\pi_2^-), & \text{otherwise} \end{cases}$$

- **Minimal invariant mass pair:**

$$m^2(D^+\pi^-)_{\mathrm{min}} = \begin{cases} m^2(D^+\pi_2^-), & \text{if } m^2(D^+\pi_1^-) > m^2(D^+\pi_2^-) \\ m^2(D^+\pi_1^-), & \text{otherwise} \end{cases}$$

This folding process reflects the symmetry by mapping events from the region above the diagonal onto the region below it, where the diagonal corresponds to $m^2(D^+\pi_1^-) = m^2(D^+\pi_2^-)$. This approach reduces the allowed region of the DP to half of its original size, effectively doubling the statistics (see Figure 7).

3.1.6 Square Dalitz Plot

In DP analyses of B-meson decays to charmless final states, both signal and background events often cluster near the kinematic boundaries due to the low masses of the final-state particles compared to the B-meson mass [4]. This clustering complicates the study of interference effects, which are primarily located near these boundaries [4]. To overcome this issue, the DP can be reshaped into a rectangular configuration, referred to as the square Dalitz plot (SDP) [21]. This transformation simplifies the analysis by expanding the regions of interference and eliminating the curved boundaries.

The transformation from the original DP to the SDP is expressed as:

$$dm^2_{ab}dm^2_{bc} \to |\det J| dm' d\theta' \tag{21}$$

where the new coordinates m' and θ' are defined as:

$$m' = \frac{1}{\pi}\arccos\left(\frac{2m_{ac} - m^{ac}_{\min}}{m^{ac}_{\max} - m^{ac}_{\min}} - 1\right) \quad \text{and} \quad \theta' = \frac{\theta_{ac}}{\pi} \tag{22}$$

Here, $m^{ac}_{\max} = M - m_b$ and $m^{ac}_{\min} = m_a + m_c$ are the kinematic limits of m_{ac}, where M is the mass of the decaying B-meson, and m_a, m_b, and m_c are the masses of the final-state particles. The helicity angle θ_{ac} describes the angle between the momenta of particles a and c, as discussed in 3.1.3.2. The term $|\det J|$ represents the determinant of the Jacobian matrix J, which accounts for the transformation of variables from the original DP to the SDP.

In this transformation, both m' and θ' range between 0 and 1, resulting in a rectangular representation of the DP. However, in the case of a symmetric DP, while m' still ranges from 0 to 1, θ' ranges from 0 to 0.5. This is because of the indistinguishability of the two final-state particles which causes any helicity angle θ_{ac} larger than $\pi/2$ to be mirrored, reducing the range of θ' to half [10].

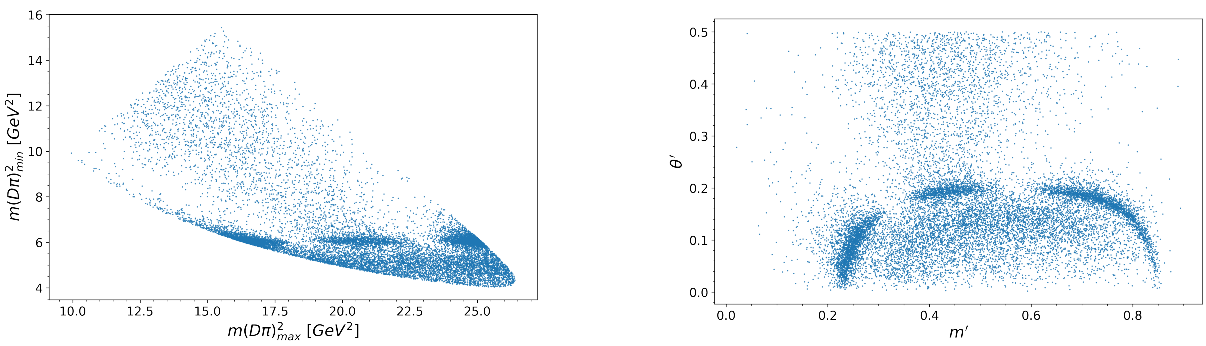

(a) Symmetric Dalitz plot (b) Squared Dalitz plot

Figure 7: Different Dalitz Plot parametrizations for $B^- \to D^+\pi^-\pi^-$ generated using an arbitrary isobar model with Laura^{++}.

3.2 Maximum likelihood fit

Experiments are conducted to infer the value of fundamental physical parameters from a series of measurements. The likelihood approach is defined as the probability of obtaining a set of observed data for given parameter values. The fit in the analysis use the extented maximum likelihood fit and the following discussion closely follow [22]. For a parameter α that follows a probability density function (PDF) $P(x|\alpha)$, and given a set of measurements $\{x_i\}$ from N independent events, the likelihood function $L(\alpha)$ is defined as the product of the individual probabilities corresponding to each measurement:

$$L(\alpha) = \prod_{i=1}^{N} P(x_i|\alpha) \tag{23}$$

where $P(x_i|\alpha)$ represents the probability of observing x_i given the parameter α. The parameter value that maximizes the likelihood function is referred to as the Maximum Likelihood Estimator (MLE) [22] of α, denoted as $\hat{\alpha}$, which provides the best estimate of the parameter α. In the maximization step, the probability density function (PDF) is normalized to one across all values of the estimator α.

In practical applications, it is often more convenient to work with the natural logarithm of the likelihood function, $F(\alpha) = -\sum_{i=1}^{n} \ln P(x_i|\alpha)$, as this transforms the product of probabilities into a sum, simplifying computations and improve machine precision.

Properties of Maximum Likelihood Estimators

MLEs should exhibit the following key properties:

1. **Unbiased:** The expected value of the estimator equals the true value of the parameter, $E[\hat{\alpha}] = \alpha_0$.
2. **Consistency:** The estimator converges to the true parameter value as the sample size increases, $\lim_{N\to\infty} \hat{\alpha} = \alpha_0$.
3. **Efficiency:** For large sample sizes, the estimator achieves the minimum possible variance.

3.2.1 Uncertainty estimation

For large datasets ($N \to \infty$), the likelihood function $L(\alpha)$ becomes approximately Gaussian. This allows us to Taylor expand the negative log-likelihood function around the minimum $\hat{\alpha}$ as:

$$F(\alpha) = F(\hat{\alpha}) + \frac{1}{2} \cdot \frac{d^2F}{d\alpha^2} \cdot (\alpha - \hat{\alpha})^2 + \dots \tag{24}$$

$$L(\alpha) \sim c \cdot \exp\left(-\frac{1}{2} \cdot \frac{d^2F}{d\alpha^2} \cdot (\alpha - \hat{\alpha})^2\right) = c \cdot \exp\left(-\frac{(\alpha - \hat{\alpha})^2}{2\sigma^2}\right) \tag{25}$$

In this limit near the maximum, the likelihood function has the form of a Gaussian function and the negative log likelihood function is parabolic, therefore the uncertainty on the parameter α, denoted as $\Delta\alpha$, can be expressed as:

$$\Delta\alpha^2 = \sigma_\alpha^2 = -\left(\frac{\partial^2 \ln L}{\partial \alpha^2}\right)^{-1}_{\alpha=\hat{\alpha}} \tag{26}$$

This allows us to express the result as $\alpha = \sigma_\alpha = \hat{\alpha} \pm \Delta\alpha$, providing an interval estimate for the parameter. The width of this interval reflects the precision of the estimate based on the observed data. This is however symmetric interval because of the negative log likelihood being parabolic. For cases where the log-likelihood function does not exhibit parabolic behavior, a nonlinear transformation of the parameter α to another parameter $z = z(\alpha)$ is necessary, such that $F(z)$ becomes parabolic. Due to the invariance of the parameter estimation in the maximum likelihood method, the best value $\hat{z}$ corresponds to $z(\hat{\alpha})$. The left and right standard deviations can be calculated as:

$$F(\hat{z} \pm \sigma_z) = F(\hat{z}) \pm \frac{1}{2} = F(\hat{\alpha}) \pm \frac{1}{2} \tag{27}$$

This approach can also be generalized to multiple parameters where the likelihood function has the form

$$L(\alpha_1, \alpha_2, \ldots, \alpha_N) = \prod_{i=1}^{n} f(x_i, \alpha_1, \alpha_2, \ldots, \alpha_N). \tag{28}$$

The covariance matrix V of the parameter vector $\boldsymbol{\alpha}$ is defined as:

$$V = G^{-1} \quad \text{with} \quad G_{ik} = \frac{\partial^2 F}{\partial \alpha_i \partial \alpha_k} \tag{29}$$

evaluated at the minimum $\hat{\alpha}$. Here, G takes the form of the Hessian matrix, and in the non-asymptotic case, the inverted Hessian matrix at the minimum serves as an approximation for the covariance matrix [22].

3.2.2 Extended Maximum Likelihood fit

In an extended maximum likelihood fit, if the probability function $P(x|\alpha)$ is no longer normalized to one, it is normalized to a function $Q(x|\alpha)$, which is defined such that its integral corresponds to the expected number of events N:

$$N = \int_\Omega Q(x|\alpha)\, dx, \tag{30}$$

where N depends on the parameter set α. Consequently, the negative log-likelihood function is given by:

$$F(\alpha) = -\sum_{i=1}^{n} \ln(Q(x_i|\alpha)) + \int_\Omega Q(x|\alpha)\, dx. \tag{31}$$

This formulation allows fitting both the shape of the distribution and the total number of expected events simultaneously.

3.2.3 Constrained Fits

In cases where a parameter in the likelihood function is known from external sources like the Particle Data Group data, this information can be incorporated into the fit. The constraint on the parameter a is characterized by a Gaussian distribution. We can include this constraint in the likelihood function as follows:

$$L(a,b) = \frac{1}{\sqrt{2\pi}\sigma_a} \exp\left(-\frac{(a-a_{\text{meas}})^2}{2\sigma_a^2}\right) \prod_i P(x_i, a, b). \tag{32}$$

Here, a_{meas} and σ_a represent the measured value of the parameter and its uncertainty, respectively. As a result, values of a closer to a_{meas} are more probable, while deviations from a_{meas} become increasingly unlikely.

3.2.4 LAURA^{++}

LAURA^{++} [16] is a C++ package designed for performing Dalitz plot fits in three-body decays of heavy-flavoured mesons to spinless final state particles, and it serves as the fitting framework for this analysis. Built on the `ROOT` framework [23], LAURA^{++} uses the `MINUIT` minimization package [24] to fit models to experimental data by minimizing the negative log-likelihood (NLL) based on the specified decay model. Error estimation is managed by `MINUIT`, providing precise uncertainties for the fitted parameters.

The fit returns the best-fit values for model parameters, such as resonance masses, widths, and the complex coefficients in the isobar model, as discussed in Section 3.1.3.1, which describe the amplitudes and phases of the decay dynamics. LAURA^{++} does not provide direct access to the parameterized fitted distribution; however, it can generate Monte Carlo (MC) toy samples based on the fitted model using the accept/reject method. The package also offers an option to perform background subtraction using *sFit* techniques.

3.3 *sFit*

sFit [25] is a statistical technique used to extract signal parameters from a dataset containing both signal and background events. It extends the *sPlot* method [26], which applies weights to events based on their likelihood of being signal or background. Using these weights, the *sFit* method constructs a likelihood function for the signal component, enabling the estimation of signal parameters without explicitly modeling the background.

sPlot and *sFit*

Suppose the variable x is uncorrelated with the discriminating variable y. The data consists of N_s signal events and N_b background events. The distributions of y for the signal and background components are denoted by $F_s(y)$ and $F_b(y)$, respectively. Assuming N_s, N_b, $F_s(y)$, and $F_b(y)$ are known, the sWeight function is defined as:

$$W_s(y) = \frac{V_{ss}F_s(y) + V_{sb}F_b(y)}{N_sF_s(y) + N_bF_b(y)}, \tag{33}$$

where V_{ss} and V_{sb} are elements of the covariance matrix V, which is obtained by inverting the following matrix:

$$V_{ij}^{-1} = \sum_{e=1}^{N} \frac{F_i(y_e)F_j(y_e)}{\left(N_sF_s(y_e) + N_bF_b(y_e)\right)^2}, \tag{34}$$

where $F_i(y_e)$ and $F_j(y_e)$ are the PDFs evaluated at y_e for the e-th event.

For each event y_e, the sWeight $W_s(y_e)$ can be calculated as above. We can then extend the *sPlot* formalism to likelihood estimation for the signal parameters by defining a weighted likelihood function. The likelihood function for a parameter θ, weighted by the sWeights, is defined as:

$$L_W(\theta) = \prod_{e=1}^{N} \left[P_s(x_e;\theta)\right]^{W_s(y_e)}, \tag{35}$$

where $P_s(x_e;\theta)$ is the probability distribution function for the signal, parameterized by θ.

The *sFit* method estimates the signal parameter θ by maximizing the weighted likelihood function $L_W(\theta)$. Since the sWeights are constructed to cancel the background contribution, the background does not affect the likelihood maximization, allowing θ to be estimated using only the signal component.

The *sFit* technique helps reduce systematic uncertainties due to an incorrect background model [25]. However, additional sources of background, such as misidentified decays, may introduce correlations between the discriminating variable and the DP variables. Therefore, this approach is only valid when such backgrounds are negligible across the entire B-candidate mass range, and not just in the signal region [16], which it is in our case.

4 Reconstruction and Selection

This section outlines the reconstruction of B meson candidates and describes the selection criteria applied to distinguish signal events from background. After reconstructing B mesons, selection criteria are applied to ensure the purity of the signal, including cut-based selection and the best candidate selection. Additionally, we discuss the DP boundary and its enforcement to handle events that fall outside the kinematically allowed region.

4.1 Simulated data at BELLE II

Simulated data plays an essential role in high-energy physics experiments, as it mimics the behavior of particles within detectors. This data, commonly referred to as Monte Carlo (MC) data, is generated to reproduce the physics processes under study. The simulation process begins with an event generator that produces particles according to a specified model, followed by a simulation of their interactions within the detector.

In the Belle II simulation workflow, multiple event generators are employed in sequence to simulate the different stages of particle interactions and decays [27]. The process typically starts with the `KKMC` generator [28], which simulates two-fermion final states, such as $\mu^+\mu^-$, $\tau^+\tau^-$, $\nu\bar{\nu}$, and $q\bar{q}$, at beam energies around and above the $\Upsilon(4S)$. Once quark pairs are generated, `PYTHIA` [29, 30] handles the hadronization process, transforming the quark pairs into hadrons through parton showers. Following hadronization, `EvtGen` [31] simulates the decays of the unstable hadrons produced in the previous phase. `EvtGen` specializes in modeling B and D meson decays, using predefined decay models and branching fractions from a decay file to ensure accurate decay simulation [11]. This file contains all possible decay channels, their branching ratios, and corresponding decay models. Finally, `PHOTOS` [32] adds final-state radiation, accounting for photon emissions from charged particles in the decay process.

After event generation, they are passed through the detector simulation using `Geant4` [33] to model the detector response. The complete events can then be fully reconstructed using the Belle II Analysis Framework (`basf2`) [34]. While `basf2` processes both real and simulated data, the key advantage of using simulated data lies in its access to MC truth information, which is unavailable in real data. This analysis uses the latest `basf2` release, `version 08-02-00`, along with the corresponding lightweight version, `light-2409-toyger`.

For this analysis, we use the MC15 run-dependent simulation samples available at Belle II. These samples, also referred to as collections, are categorized into two main types: signal MC and generic MC. Signal MC consists of the specific decay samples under analysis, while generic MC includes known B-meson decay channels. The generic MC samples are further divided into charged (B^+B^-) and mixed ($B^0\bar{B}^0$) collections, with each corresponding to 699.235 fb^{-1} of simulated data.

A major source of background arises from continuum events, which are $e^+e^- \to q\bar{q}$, where $q = u, d, s, c$. There are four collections, one for each type of quark, with each representing 699.235 fb^{-1} of simulated data. These continuum samples are generated using `PYTHIA`.

Due to the low branching ratio of the decay $B^- \to D^+\pi^-\pi^-$, the resulting statistics are limited. To address this, we generate high-statistics signal MC samples using `EvtGen` for various tasks, such as studying efficiency effects. Additionally, these samples can be used to validate fit results by generating events at the generator level (without detector simulation).

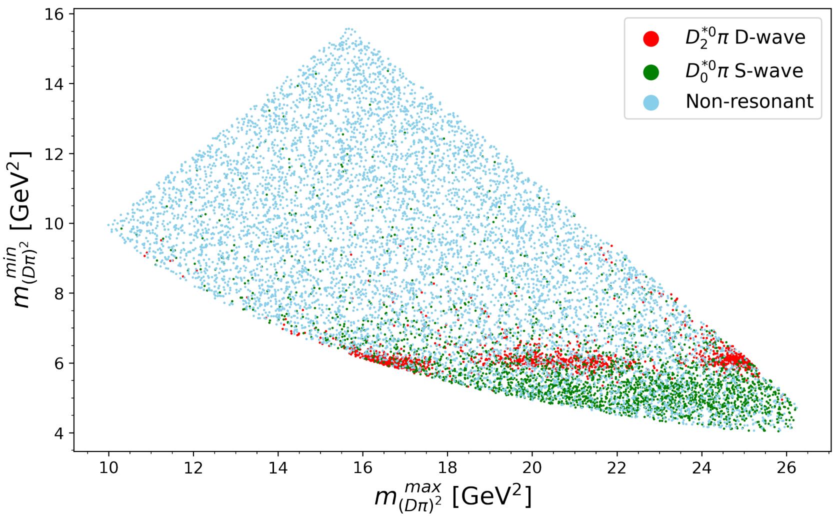

(a)

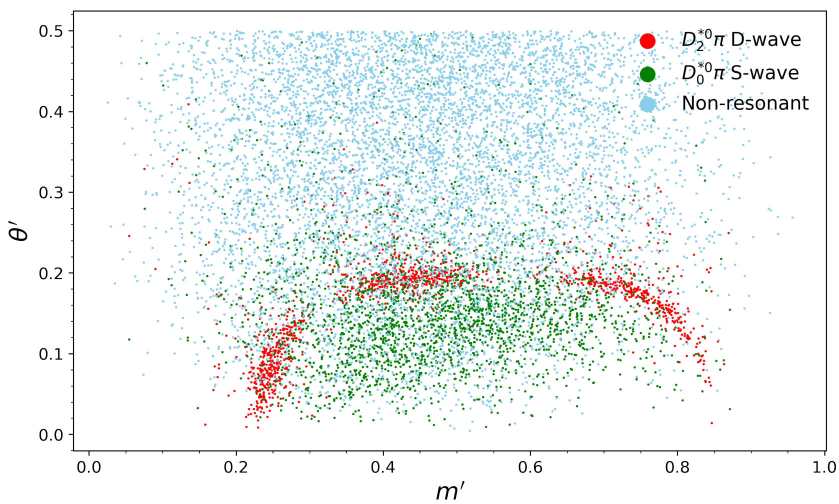

(b)

Figure 8: The signal component, separated into its constituents—D_2^0, D_0^0, and a non-resonant contribution—is shown in both (a) the Symmetric DP and (b) the square DP.

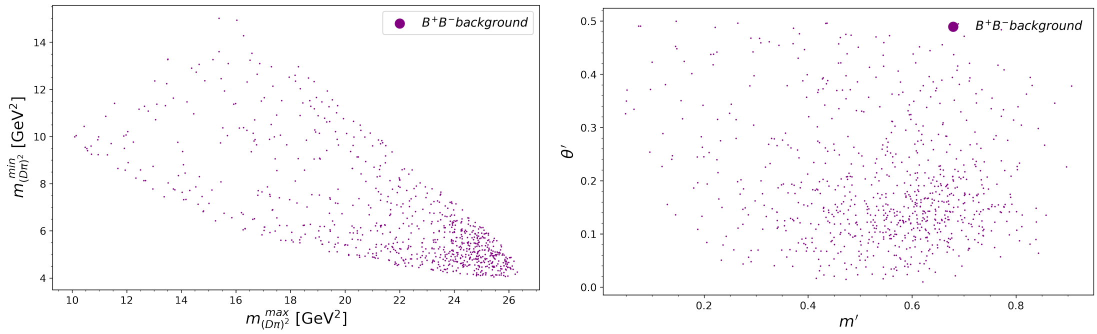

(a) (b)

Figure 9: Charged background samples from equally sized generic MC, with the signal component removed, are shown in the symmetric DP (a) and square DP (b), respectively.

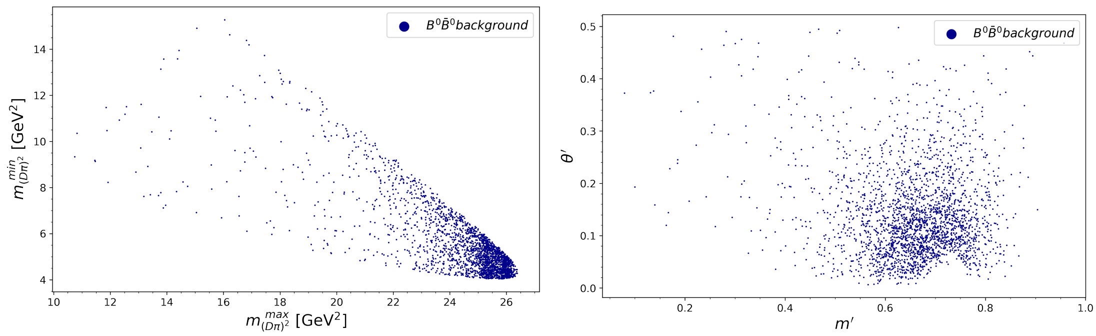

(a) (b)

Figure 10: Neutral background samples from equally sized generic MC are shown in the symmetric DP (a) and square DP (b), respectively.

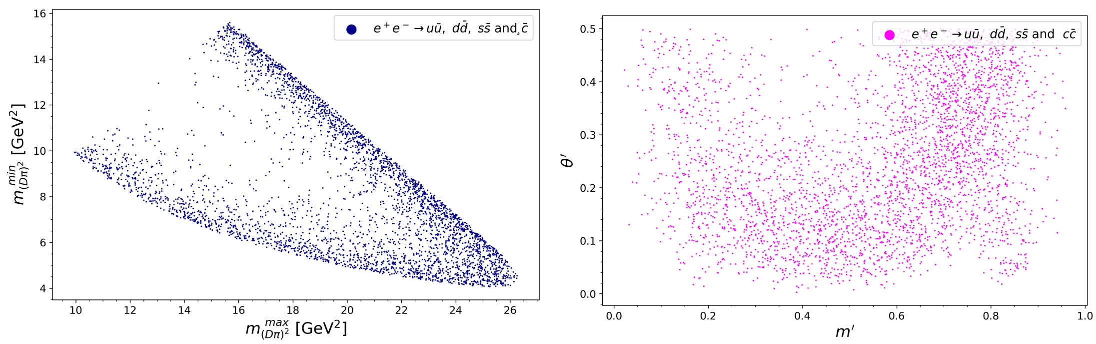

(a) (b)

Figure 11: Continuum background samples from equally sized MC, for each c, u, d and s components, are shown in the symmetric DP (a) and square DP (b), respectively.

4.2 Reconstruction of B Meson Candidates

In this section, we reconstruct charged B-meson candidates by running a steering file on the MC data, as explained in Section 4.1, using basf2 [34], and apply selection criteria. The reconstruction follows a hierarchical approach, where final-state particle candidates are first constructed from reconstructed tracks and clusters [35]. These candidates are then combined to form intermediate particles, which are subsequently combined to produce the final B-meson candidates for the decay $B^- \to D^+\pi^-\pi^-$. At each stage of this process, specific selection criteria must be met. The selection procedure is divided into two phases: 'online' and 'offline' selection. The online selection is applied during the initial processing of simulated Monte Carlo (MC) data to retain all possible signal events, while the offline selection applies finer cuts to improve signal purity.

4.2.1 Reconstruction Channel

For this analysis, we reconstruct the exclusive decay $B^- \to D^+\pi^-\pi^-$ and its charge-conjugate mode. The D^+ meson is reconstructed via the decay $D^+ \to K^-\pi^+\pi^+$, which is the most frequent hadronic decay mode of the D^+ meson [10]. In doing so, we follow [10, 8, 1].

4.2.2 Final-State Particles

The relevant final states for this analysis are $\pi^\pm$ and $K^\pm$. The charged tracks of these final-state particles are subjected to selection criteria during the online selection phase. The identification of pions and kaons is critical to the analysis, relying on probabilities derived from information provided by detectors such as the CDC and TOF [36].

- **pionID**: The probability of a track being identified as a pion.
- **kaonID**: The probability of a track being identified as a kaon.

The likelihood values for particle identification are constructed as follows [10, 11]:

$$PID_{\pi/K} = \frac{L(\pi)}{L(\pi) + L(K)}, \quad PID_{K/\pi} = \frac{L(K)}{L(\pi) + L(K)} = 1 - PID_{\pi/K} \tag{36}$$

In addition to PID, kinematic variables are used to refine track selection:

- **dr**: The transverse distance of the point of closest approach (POCA) with respect to the interaction point (IP).
- **dz**: The z-component of the POCA with respect to the IP.

Another variable used is nCDCHits, which represents the number of CDC hits associated with the track. The following constraints were applied to the final-state particles during the online selection:

Variable	$\pi^\pm$	$K^\pm$
PID	pionID > 0.3	kaonID > 0.6
|dr|	< 2 cm	< 2 cm
|dz|	< 4 cm	< 4 cm
nCDCHits	> 20	> 20

Table 2: Online selection cuts applied to the final-state particles.

4.2.3 D-Meson Reconstruction

The final-state particles that meet the selection criteria from Table 2 are combined to form D^+ candidates from $K^-\pi^+\pi^+$ combinations. During the online selection, the invariant mass of the D^+ candidates is required to lie within the interval $[1.83965, 1.89965]$ GeV$/c^2$, corresponding to a 60 MeV window around the nominal D^+ mass of 1.869 GeV$/c^2$.

4.2.4 B-Meson Reconstruction

The final step in the reconstruction process involves combining the D meson and final-state particles to form a B meson. Each B meson carries half of the total beam energy in the center-of-mass frame [11]. Two key variables used to identify B mesons are the beam-constrained mass M_{bc} and the energy difference ΔE.

The beam-constrained mass M_{bc} is defined as:

$$M_{bc} = \frac{1}{c^2}\sqrt{E^{*2}_{\text{Beam}} - c^2\left(\sum_i \vec{p}_i\right)^2}, \tag{37}$$

where E^*_{Beam} is half of the total beam energy in the $\Upsilon(4S)$ center-of-mass frame, and $\vec{p}_i$ are the momenta of the B-meson candidate's daughter particles. A properly reconstructed B meson will peak at the nominal mass of the B meson.

The energy difference ΔE is calculated as:

$$\Delta E = \sum_i \sqrt{c^2 p_i^2 + c^4 m_i^2} - E^*_{\text{Beam}}, \tag{38}$$

where p_i and m_i are the momenta and masses of the B-meson candidate's daughter particles, and E^*_{Beam} is the beam energy. This variable checks whether the energy of the reconstructed B meson matches the beam energy. For a properly reconstructed B meson $\Delta E = 0$.

During the online selection, the following cuts are applied: $|\Delta E| < 0.25$ GeV and $M_{bc} > 5.24$ GeV$/c^2$.

4.2.5 Vertex Reconstruction

Vertex reconstruction is used to accurately determine the decay vertex or interaction vertex of particles based on the reconstructed parameters of the outgoing particles. This process ensures that the reconstructed daughter particles originate from the same vertex. In this analysis, the `TreeFitter` algorithm [37] is employed to fit entire decay chains. `TreeFitter` globally parameterizes the decay tree, enabling information sharing across the entire decay structure [11]. The fit minimizes the χ^2 value, which is constructed from the track parameters and their corresponding error matrices [10]. Candidates for which the vertex fit fails are rejected.

The vertex fit reduces the migration of B meson candidates, preventing the points on the DP from drifting away from their true positions. In this analysis, a mass-constrained fit is performed on the reconstructed B meson, and the invariant masses of the B meson's daughter particles are updated. Therefore, before the vertex fit, selection criteria are applied, and the updated variables are subsequently used in the DP fit.

4.3 Selection of B Meson Candidates

Following the reconstruction and online selection of B mesons, additional offline selection cuts are applied to further reduce background and enhance the signal-to-background ratio. The offline selection consists of the following steps, detailed below:

- **Cut-based selection** - applying specific kinematic and mass constraints to refine the selection of B meson candidates.
- **Best candidate selection** - selecting the best candidate per event and per decay channel.

4.3.1 Cut-based Selection

In this analysis, a cut-based selection method is used to isolate B-meson candidates and enhance the signal-to-background ratio. Several kinematic cuts are applied to ensure the reconstruction of well-defined B meson candidates while reducing background contamination. These cuts are summarized in Table 3.

Cut Variable	**Cut Value**
M_{bc}	$M_{bc} > 5.27$ GeV/c^2
M_{D+}	$1.85865 < M_{D+} < 1.88065$ GeV/c^2
ΔE	$-0.025 < \Delta E < 0.025$ GeV
M	$5.26 < M < 5.30$ GeV/c^2

Table 3: Offline selection cuts for B meson candidates.

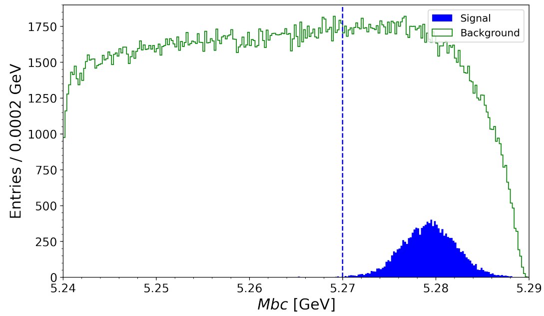

(a) $M_{\rm bc}$ after the online selection

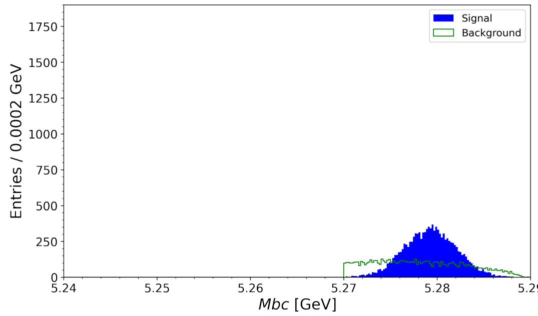

(b) $M_{\rm bc}$ after the offline selection

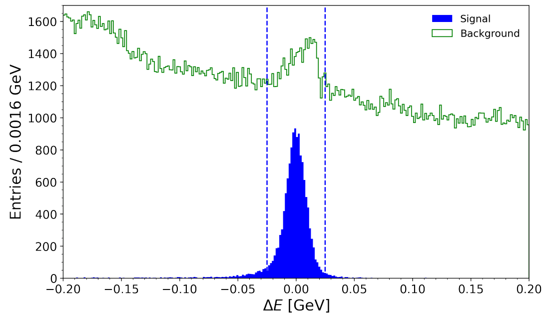

(c) ΔE after the online selection

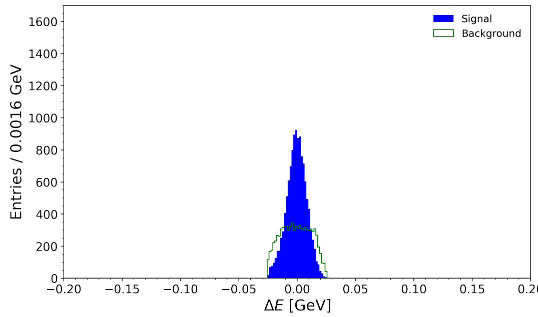

(d) ΔE after the offline selection

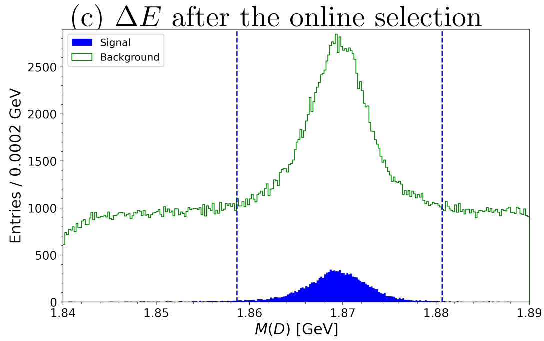

(e) $M(D)$ after the online selection

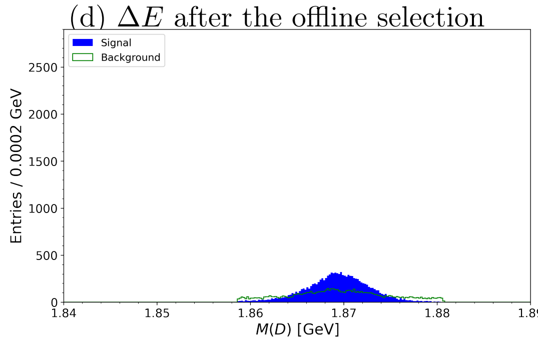

(f) $M(D)$ after the offline selection

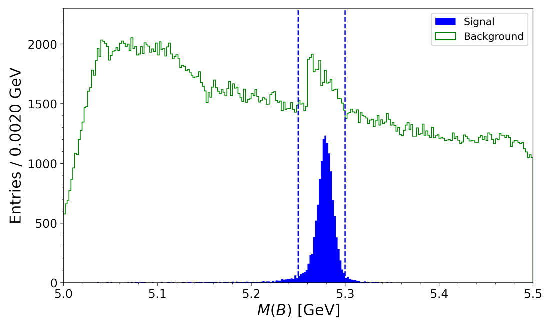

(g) $M(B)$ after the online selection

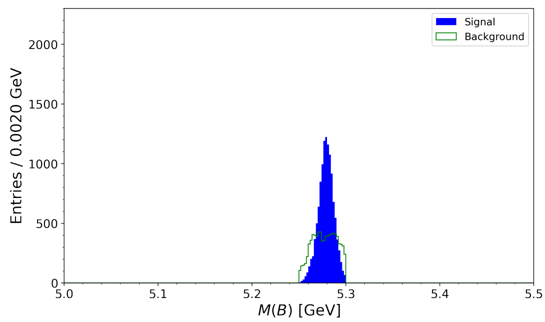

(h) $M(B)$ after the offline selection

Figure 12: Distributions of variables $M_{\rm bc}$, ΔE, $M(D)$, and $M(B)$ after the online and offline selection stages. Each pair of plots illustrates the effects of these selection processes on the corresponding variable.

In this analysis, the signal is defined as events originating from the D_2^{*0}, D_0^{*0}, and non-resonant contributions, as shown in figure 8, while all other events are considered as background. The following MC flags are used to categorize these events for further analysis:

- `isSignal`: Used to separate signal events from background events.
- `isContinuumEvent`: Identifies continuum background events ($e^+e^- \to q\bar{q}$).
- `genMotherPDG`: Differentiates between various signal components, such as contributions from D_2^{*0}, D_0^{*0}, and non-resonant events.

Although the MC flags are not involved in the event selection process itself, they are useful for classifying events, validating fits, and visualizing the composition of the selected data.

4.3.2 Best Candidate Selection

In the reconstruction process of B mesons, multiple B-meson candidates may be found in a single event. Since only one B meson can be correctly reconstructed per event, selecting the best candidate is crucial to avoid misreconstructed events. While optimized criteria, such as ΔE or M_{bc}, could be used to select the best candidate and potentially reduce background, such methods may introduce bias by altering the distributions of these variables. To prevent this, the analysis adopts a random selection approach, where a single candidate is randomly chosen from the available candidates in each event. This method ensures no preferential selection based on ΔE or M_{bc}, preserving the integrity of these distributions for use in later stages of the analysis.

4.3.3 Dalitz Plot Boundary

In this analysis, some events are reconstructed outside the allowed DP boundary, even after performing a B mass-constrained vertex fit. Events falling outside the physical DP boundary typically result from detector effects, combinatorial mistakes, or misreconstruction during the analysis [10]. For these candidates, the likelihood values for both signal and background events become zero, as they violate the kinematic constraints of the system. These events also create complications when fitting the DP using Laura^{++}.

To mitigate this issue, only candidates that lie within the physical DP boundary are included in the analysis. This is enforced by applying the DP boundary condition, as shown in equation 2. The effect of this constraint can be seen in Figure 13.

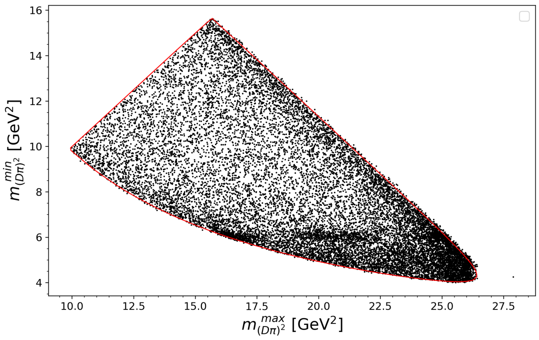

(a)

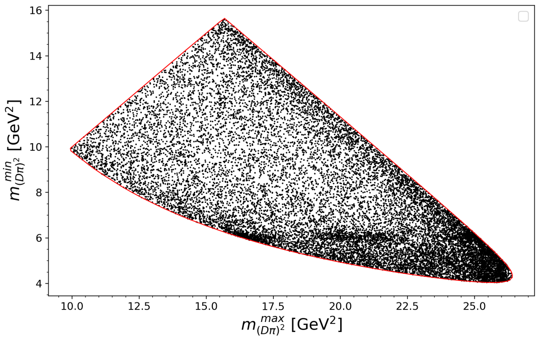

(b)

Figure 13: Comparison of distributions in the Dalitz plot before (a) and after (b) applying the DP boundary constraint. (a) shows events outside the allowed Dalitz plot boundary, likely due to detector effects, combinatorial mistakes, or misreconstruction. (b) shows only candidates that lie within the physical Dalitz plot boundary.

Component	No. Candidates
Signal	11751
Background	6998

Table 4: The number of B candidates after the finalized offline selection of individual components.

5 Background Subtraction

Building on the discussions from Section 3.3, where the *sPlot* technique was introduced, this section explains how *sPlot* is used to statistically subtract background contributions without requiring explicit background modeling in the DP. The *sPlot* method allows for the calculation of sWeights, which are essential for separating signal from background events. These sWeights are derived from a fit to a discriminating variable, which, in this analysis, is the beam-constrained mass M_{bc}.

Signal and Background Modeling

For the *sFit* method to be effective, the discriminating variable M_{bc} must be uncorrelated with the DP variables. To validate this assumption, the Kendall τ coefficient [38] is used. Kendall's τ measures the correlation between two variables, ranging from -1 (perfect negative correlation) to 1 (perfect positive correlation), with a value of 0 indicating no correlation.

After confirming that M_{bc} is uncorrelated, see Figure 14, the signal and background components (4.3.1) are modeled using PDFs, with the beam-constrained mass M_{bc} ranging from 5.27 to 5.29 GeV. The combined model, consisting of both the Gaussian signal and the Argus background, was fitted to the dataset using a maximum likelihood approach, as discussed in Section 3.2.

The Gaussian PDF for the signal is defined as:

$$\text{Gaussian}(M_{bc}, \mu, \sigma) = \frac{1}{\sqrt{2\pi}\sigma} \exp\left(-\frac{(M_{bc}-\mu)^2}{2\sigma^2}\right), \tag{39}$$

where $\mu = 5.27933 \pm 0.00004\,\text{GeV}$ is the mean, and $\sigma = 0.00291 \pm 0.00004\,\text{GeV}$ is the width of the distribution.

For the background, the Argus function is defined as:

$$\text{Argus}(M_{bc}, m_0, c, p) = \mathcal{N} \cdot M_{bc} \cdot \left[1 - \left(\frac{M_{bc}}{m_0}\right)^2\right]^p \cdot \exp\left[c \cdot \left(1 - \left(\frac{M_{bc}}{m_0}\right)^2\right)\right], \tag{40}$$

where $m_0 = 5.2892 \pm 0.00002\,\text{GeV}$ is the cutoff parameter, $c = -41.4292 \pm 11.0803$ is the shape parameter, and $p = 1$.

After fitting the model to the data, we evaluated the fit quality using the χ^2 statistic, obtaining a value of

$$\chi^2 = 37.819,$$

which suggests a reasonable fit between the model and data. The resulting signal yield was $n_{\text{signal}} = 12,551 \pm 120.7$, while the background yield was $n_{\text{background}} = 5,991.7 \pm 130.5$, differing from the expected yields presented in Table 4. This discrepancy could potentially introduce a minor bias in the sWeights, which influence the background subtraction process.

To further assess the accuracy of background subtraction, we examined the pull distribution, with the pull defined in Equation 44 and illustrated in Figure 16. Ideally, the pull distribution should be centered around zero, with most values within the ± 1 range. However, some bins near the left kinematic boundary show pulls exceeding ± 3. This deviation is attributed to an overestimated signal yield, as discussed above, as evident in Figure 16.

Utilization of sWeights in Laura^{++}

Following the fit, sWeights were calculated as described in Section 5 and stored in a `ROOT` file for signal and background contributions, enabling a clear separation of the signal and background components.

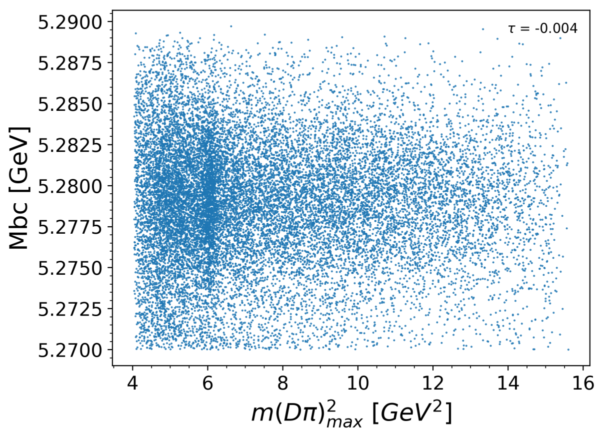

(a)

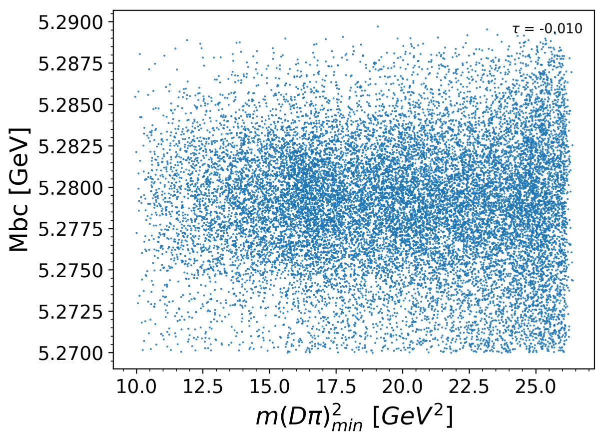

(b)

Figure 14: Scatter plot for Mbc and (a) $m(D\pi)_{\max}$ and (b) $m(D\pi)_{\min}$ with the Kendall's Tau coefficient.

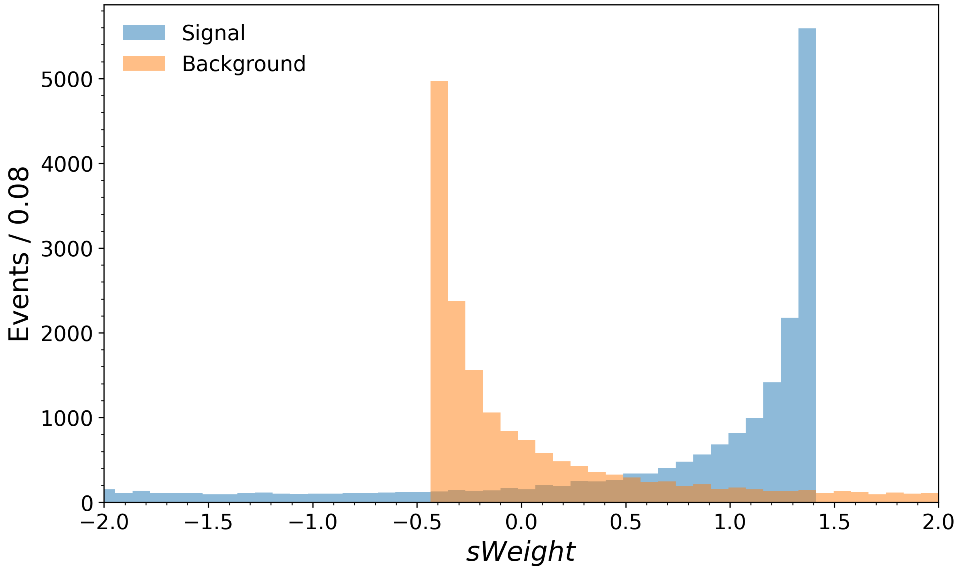

Figure 15: Distribution of sWeights for the signal component.

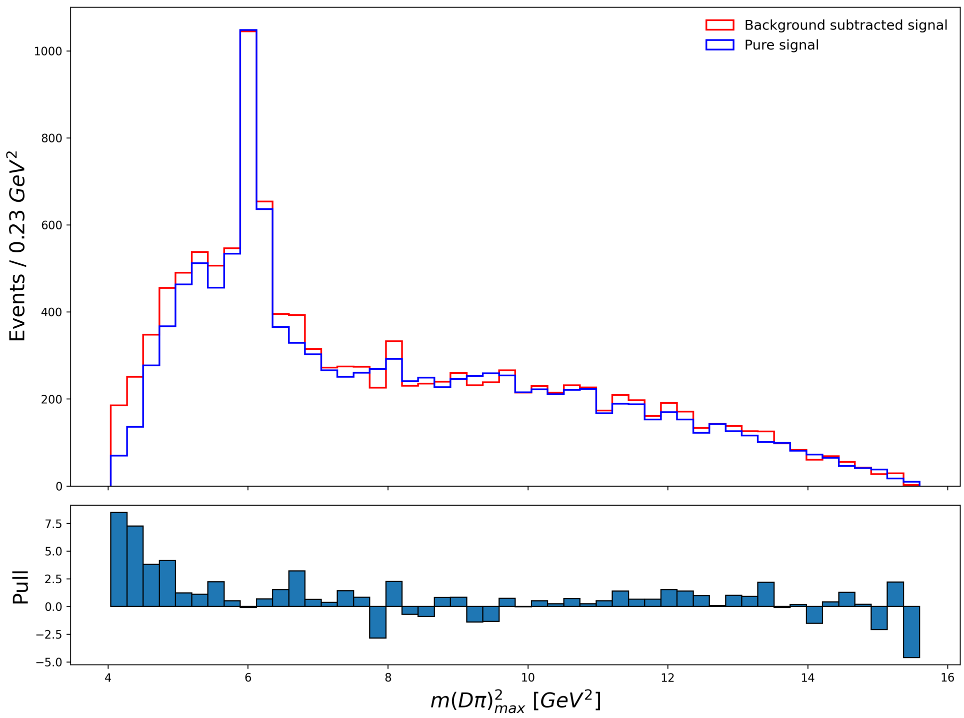

Figure 16: Comparison between weighted data and pure signal with pull distribution.

6 Detector Efficiency

In the absence of reconstruction effects, the DP probability density function is given by:

$$P_{\text{phys}}(m_{13}^2, m_{23}^2) = \frac{|A(m_{13}^2, m_{23}^2)|^2}{\int\int_{\text{DP}} |A(m_{13}^2, m_{23}^2)|^2 \, dm_{13}^2 \, dm_{23}^2}, \tag{41}$$

where $A(m_{13}^2, m_{23}^2)$ is the amplitude for the given decay mode. However, in practice, the detector influences the reconstructed events, altering the observed distribution on the DP. This effect is especially significant in Dalitz analyses, as the kinematics vary depending on the position in the Dalitz plane [4]. The efficiency, denoted as $\epsilon(m_{13}^2, m_{23}^2)$, defines the probability of reconstructing and selecting an event at a given point in the phase space, assuming it was generated there.

To account for efficiency, a bin-wise ratio is computed across the DP. A large sample of non-resonant signal MC events, uniformly distributed across the Dalitz plane, is generated and passed through a full detector simulation using `Geant4`. These events undergo the full selection criteria outlined in Chapter 4. The overall efficiency for each individual bin i is determined as:

$$\epsilon_i(m_{13}^2, m_{23}^2) = \frac{N_{\text{reco},i}}{N_{\text{gen},i}}, \tag{42}$$

where $N_{\text{reco},i}$ represents the number of events in bin i that were successfully reconstructed, and $N_{\text{gen},i}$ is the number of events generated in bin i. It is essential to acknowledge the possibility of migration, where events generated in bin i may migrate to another bin j, or vice versa. This migration is considered minimal due to the vertex fitting procedure applied to the reconstructed B meson, as described in Section 4.2.5, and is therefore not included in this analysis.

The signal PDF, originally defined in Eq. 41, is modified as follows:

$$P_{\text{sig}}(m_{13}^2, m_{23}^2) = \frac{|A(m_{13}^2, m_{23}^2)|^2 \epsilon(m_{13}^2, m_{23}^2)}{\int\int_{\text{DP}} |A(m_{13}^2, m_{23}^2)|^2 \epsilon(m_{13}^2, m_{23}^2) \, dm_{13}^2 \, dm_{23}^2}. \tag{43}$$

The binning of the DP is a crucial factor in accurately estimating efficiency, as bins near the DP boundaries may be sparsely populated. In the standard Dalitz plane representation, although events are uniformly distributed, some bins near the edges may cross kinematic boundaries, resulting in lower populations compared to the bins located in the center [36]. To mitigate this, the analysis employs the SDP representation, $\epsilon(m', \theta')$, which transforms the DP into a rectangular shape, resolving the issue of bins crossing boundaries. However, this transformation introduces non-uniformity in the event distribution, and the efficiency tends to decrease towards the edges, as one of the final-state particles is produced at rest in the frame of the decaying particle [4]. An appropriate binning scheme is therefore necessary. A binning of 10×10 was selected, corresponding to a bin width of

0.1×0.05. To minimize statistical fluctuations due to limited event statistics, cubic spline fitting is applied to smooth the efficiency distributions across the DP, thereby effectively changing the binning to 400×400, corresponding to a bin width of 0.0025×0.00125.

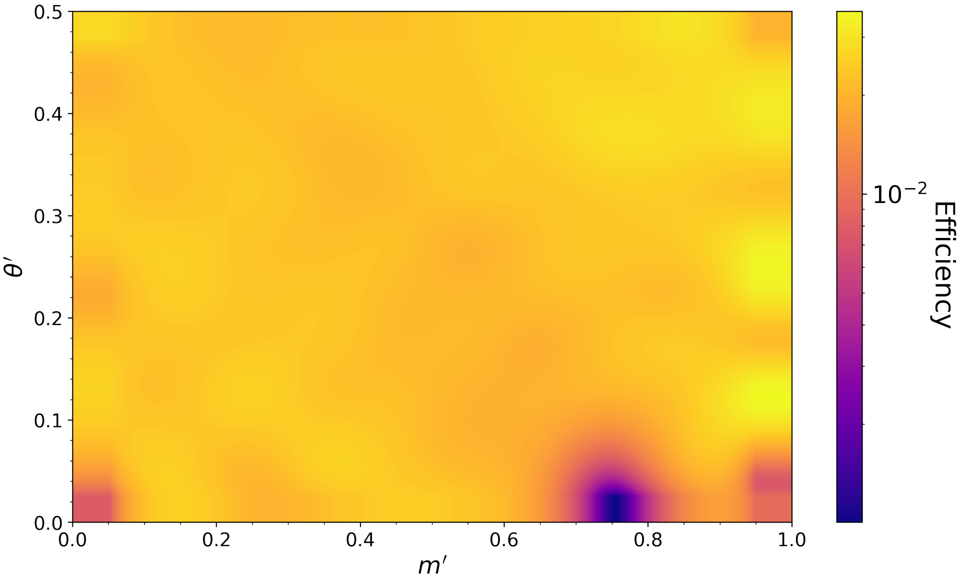

(a) Efficiency plot with log scale

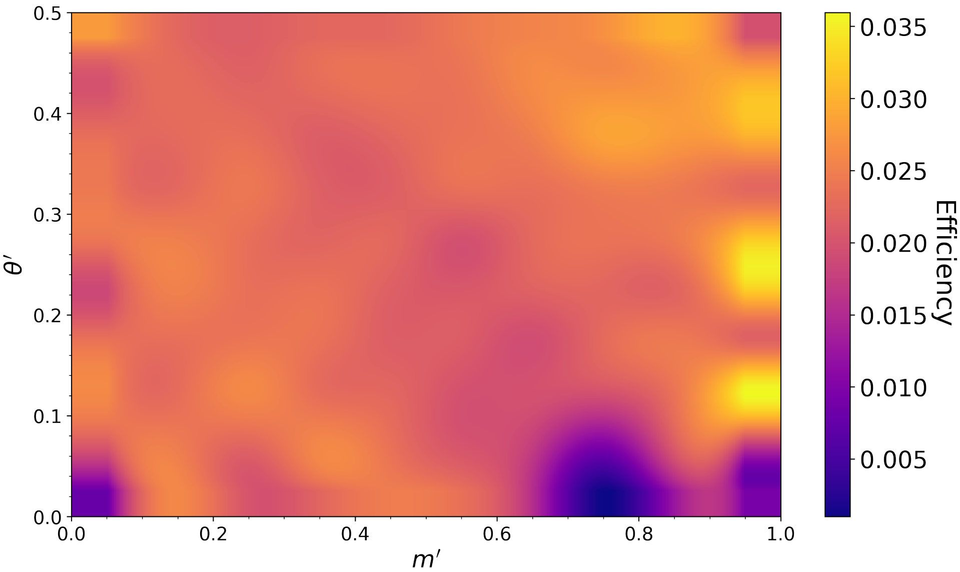

(b) Efficiency plot without log scale

Figure 17: Comparison of efficiency plots with and without log scaling for better visualization of data across orders of magnitude.

7 Fit Model

The fit model for this analysis includes contributions from resonant structures and a non-resonant component. To properly account for detector efficiency, as discussed in Chapter 6, a 2D efficiency histogram is incorporated into the fitting framework. Additionally, background subtraction is handled by applying the s-weights calculated in Chapter 5. The components of the fit model are described as follows:

- **Signal Model:** The signal model includes two resonant states, D_2^{*0} and D_0^{*0}, along with a non-resonant component. Both the D_0^{*0} and D_2^{*0} resonances are modeled as relativistic Breit-Wigner (RelBW) functions, with mass, width, and form factor parameters specified in Table 5. A non-resonant contribution is included, modeled with a flat distribution (FlatNR) across the DP.

- **Efficiency:** A uniformly binned 2D histogram of efficiency, $\epsilon_i(m', \theta')$, calculated in Chapter 6, is provided as a `ROOT` histogram and utilized in LAURA^{++} via the `LauEffModel` class [16]. While efficiency maps would typically be needed for each background component, this analysis employs a background subtraction method, requiring an efficiency map only for the signal.

- **sWeights:** The sweights calculated in chapter 5 are included with the input data, containing all components (signal and background: mixed, neutral, and combinatorial). These weights are incorporated into LAURA^{++} using the sPlot formalism, which is implemented via the `LauAbsFitModel` class with the `doSFit()` function [16].

Table 5: Signal Components: Spin, Mass, Width, Form Factor, and Model

Parameter	D_0^{*0}	D_2^{*0}	Non-Resonant
Spin	0	2	0
Mass (GeV)	2.300	2.4607	-
Width (GeV)	0.270	0.0475	-
Form Factor (GeV^{-1})	-	4.0	-
Model	RelBW	RelBW	FlatNR

The resonance parameters for each component, including resonance masses and widths, are optimized within the fit. The D_2^{*0} amplitude is chosen as the reference amplitude, with its real and imaginary components fixed to 1 and 0, respectively, facilitating a meaningful interpretation of the decay amplitude. In this analysis, we represent the amplitude in terms of its real and imaginary parts, as described in Section 3.1.4. This approach has been shown to be more stable than using amplitude and phase representation.

8 Fit Validation

The fit model was validated with a focus on two key aspects: accurately capturing detector efficiency effects and reliably reproducing input values without introducing bias. To confirm that the constructed efficiency histogram, as described in Chapter 6, accurately represents the detector's influence on observed distributions, validation was conducted using MC samples generated with full detector simulation. Individual resonance samples of 20,000 events each were generated using `EvtGen`, with resonance parameters specified in Table 5, and detector response was simulated with `Geant4`. To assess the model's robustness and ensure it remains unbiased across different input values, ensemble tests were conducted by generating and fitting "random model" samples.

8.1 Fit Validation with Individual Resonances

To validate whether the fit framework accounts for detector effects correctly, fits were conducted on truth-matched signal MC samples for the resonances D_0^{*0} and D_2^{*0}. In each fit, the amplitude and phase of the resonance under consideration were fixed to 1.0 and 0.0, respectively, while other components were allowed to float, following the methodology outlined in [10] and [36]. Projections of the fitted signal shapes onto the DP variables $m(D\pi)_{\min}$ and $m(D\pi)_{\max}$, were compared to the generated shapes to evaluate model accuracy.

To quantify the deviation of the fit result from the input, we use the pull distribution, where the pull for bin i is defined as

$$\text{pull}_i = \frac{N_{i,\text{fitted}} - N_{i,\text{generated}}}{\sqrt{N_{i,\text{fitted}}}}. \tag{44}$$

where $N_{i,\text{fitted}}$ is the fitted value of the parameter, $N_{i,\text{generated}}$ is the true or generated value of the parameter and $\sqrt{N_{i,\text{fitted}}}$ is the uncertainty of $N_{i,\text{fitted}}$, assuming Poisson statistics.

Figure 18 and 19 presents the projections of DP variables and fitted variables and corresponding pull distribution for D_0^{*0} and D_2^{*0}, respectively.

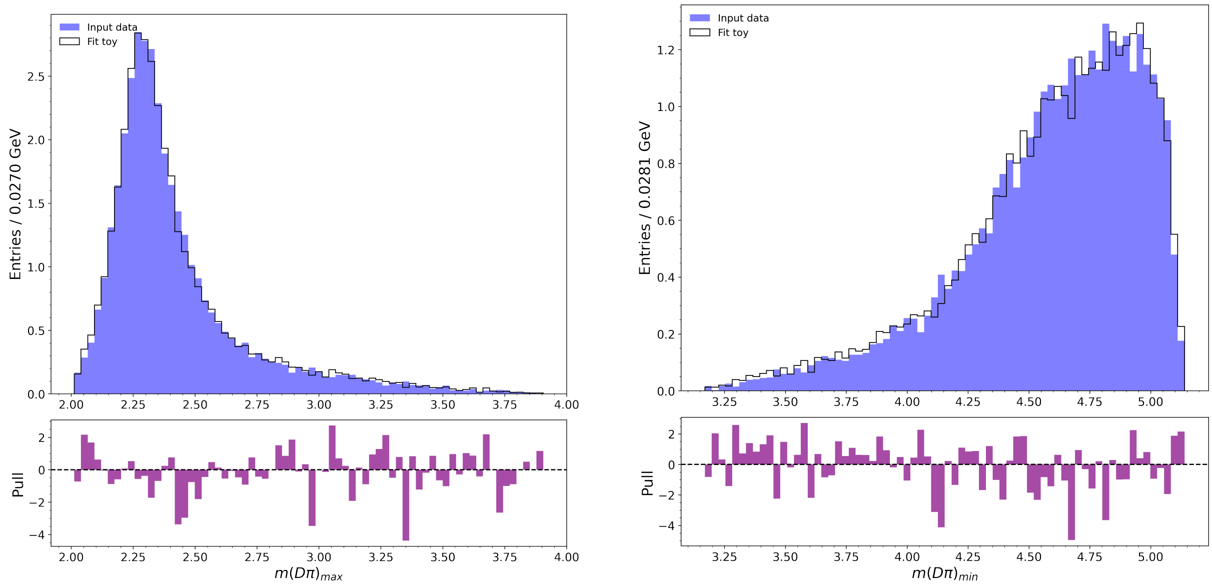

(a) (b)

Figure 18: Comparison of fitted and signal MC projections for D_0^{*0} onto $m(D\pi)_{\text{max}}$ and $m(D\pi)_{\text{min}}$, with corresponding pull distributions.

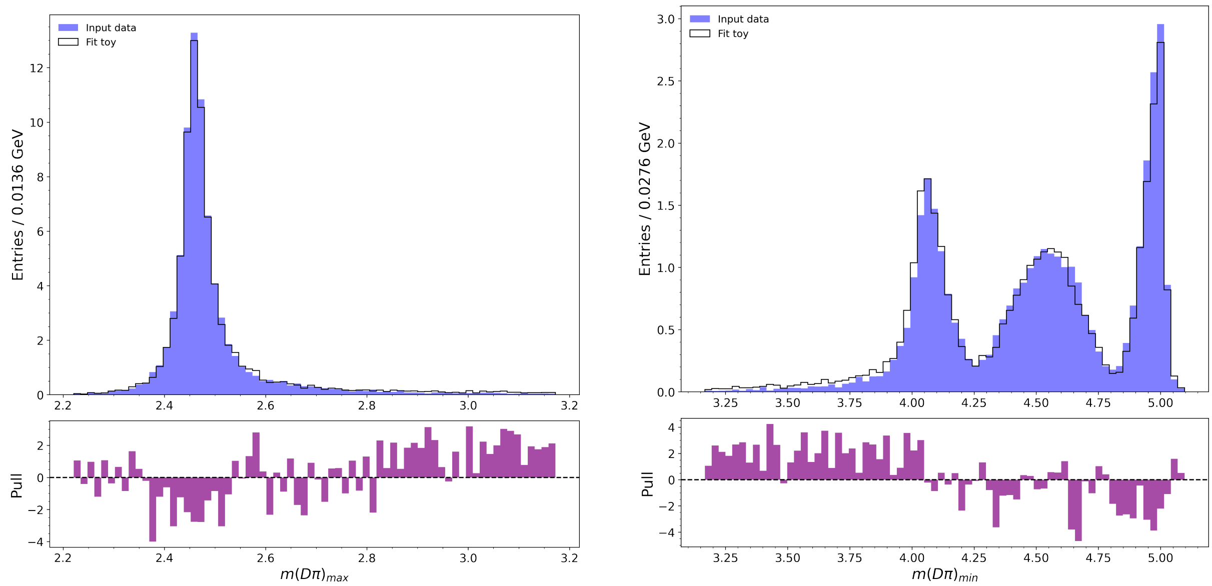

(a) (b)

Figure 19: Comparison of fitted and signal MC projections for D_2^{*0} onto $m(D\pi)_{\text{max}}$ and $m(D\pi)_{\text{min}}$, with corresponding pull distributions.

The results of the fit validation demonstrate that the fit framework effectively fit the input signal MC for D_0^{*0} and D_2^{*0}, as evidenced by the consistency in the pull distributions and the agreement in the projections of $m(D\pi)_{\text{min}}$ and $m(D\pi)_{\text{max}}$. These results confirm that the fit framework accurately accounts for detector effects.

8.2 Fit Validation by Ensemble Tests

To assess the fit model's robustness in capturing various input values without introducing biases, ensemble tests were performed. To do this, we follow the methodology outlined in the ensemble tests chapter from [10].These tests involved generating multiple random, physically realistic scenarios using LAURA^{++} and refitting them to evaluate potential biases due to the fitting framework. The random models were based on the current world averages of branching fractions from the PDG [5].

A coherent isobar model was used to simulate events with random combinations of amplitudes and phases. Each channel's amplitude was defined by a complex coefficient with real and imaginary components, weighted by relative branching ratios. These weights (α, β, and γ) were sampled from normal distributions centered around the PDG branching fractions for each channel, along with their uncertainties. The phases ϕ_α and ϕ_β were drawn from a uniform distribution $U(-\pi, \pi)$.

The total amplitude A_{tot} is given by:

$$A_{\text{tot}} = \alpha e^{i\phi_\alpha} A_{\text{NonRes}} + \beta e^{i\phi_\beta} A_{D_0^*} + \gamma A_{D_2^*}, \tag{45}$$

where $A_{\text{NonRes}}, A_{D_0^*}$, and $A_{D_2^*}$ represent the amplitudes of the non-resonant, D_0^*, and D_2^* channels, respectively. Since LAURA++ normalizes each amplitude independently, the relative weights α, β, and γ are calculated from the PDG branching ratios B_i, such that $A_i \sim \sqrt{B_i}$, normalized to the inclusive branching fraction B_{inc}[10]:

$$\alpha = \sqrt{\frac{B_{\text{NonRes}}}{B_{\text{inc}}}}, \tag{46}$$

$$\beta = \sqrt{\frac{B_{D_0^*}}{B_{\text{inc}}}}, \tag{47}$$

$$\gamma = \sqrt{\frac{B_{D_2^*}}{B_{\text{inc}}}}. \tag{48}$$

Fits were performed on 300 Monte Carlo samples generated using this random model. Tables 7-10 report the results, with the number of floating parameters varying across tests. The amplitude is represented in terms of real (X) and imaginary (Y) components. The real part of D_2^*'s amplitude, $X_{D_2^*}$, is fixed at a random value (0.354, for the random model below), while the imaginary part $Y_{D_2^*}$ is set to zero as a reference. All 300 fits succeeded, verifying the model's stability across configurations.

- **Ensemble 1**: Only the minimal set of free parameters is used, with all resonance parameters fixed.
- **Ensemble 2**: The resonance parameters of the D_2^{*0} component, including its mass

Parameter	X	Y	Mass	Width
NonRes	0.042	0.366	-	-
D_2^{*0}	0.354	0.000	2.4626	0.049
D_0^{*0}	0.226	0.161	2.318	0.267

Table 6: True values for the parameters of the random model.

and width, are floated, along with the coefficients of the isobar model.

- **Ensemble 2**: The resonance parameters of the D_0^{*0} component, including its mass and width, are floated, along with the coefficients of the isobar model.
- **Ensemble 3**: Both the mass and width of the D_0^* and D_2^* resonances are floated, along with the coefficients of the isobar model.

For each ensemble, the fit results for the parameters of interest are evaluated against the true input values by calculating the mean and width of the pull distributions. An unbiased fit with accurate uncertainty estimates should produce pull distributions centered at zero with a width of approximately one. By examining the mean and width of these pulls across the three ensemble tests, we can assess the presence of any systematic biases that may indicate a need for correction in the fit model.

Fit Parameter	Entries	Pull Mean	Pull Width
$X_{D_0^{*0}}$	300	0.059 ± 0.064	0.989 ± 0.050
$Y_{D_0^{*0}}$	300	-0.073 ± 0.060	0.893 ± 0.056
X_{NonRes}	300	-0.106 ± 0.059	0.916 ± 0.045
Y_{NonRes}	300	-0.065 ± 0.058	0.936 ± 0.052

Table 7: Ensemble 1 fit validation results,with all resonance parameters fixed.

Fit Parameter	Entries	Pull Mean	Pull Width
$X_{D_0^{*0}}$	300	-0.109 ± 0.065	1.001 ± 0.055
$Y_{D_0^{*0}}$	300	-0.029 ± 0.060	0.955 ± 0.050
X_{NonRes}	300	-0.041 ± 0.061	0.972 ± 0.047
Y_{NonRes}	300	-0.046 ± 0.054	0.852 ± 0.042
$m(D_2^{*0})$	300	0.236 ± 0.179	0.152 ± 0.238
$\Gamma(D_2^{*0})$	300	0.304 ± 0.298	0.249 ± 0.393

Table 8: Ensemble 2 fit validation results, with floating D_2^{*0} mass and width.

Fit Parameter	Entries	Pull Mean	Pull Width
$X_{D_0^{*0}}$	300	-0.026 ± 0.063	1.025 ± 0.048
$Y_{D_0^{*0}}$	300	0.043 ± 0.061	0.992 ± 0.049
X_{NonRes}	300	-0.038 ± 0.062	0.962 ± 0.047
Y_{NonRes}	300	0.062 ± 0.054	0.887 ± 0.040
$m(D_0^{*0})$	300	0.236 ± 0.179	0.152 ± 0.238
$\Gamma(D_0^{*0})$	300	0.304 ± 0.298	0.249 ± 0.393

Table 9: Ensemble 3 fit validation results, with floating D_0^{*0} mass and width.

Fit Parameter	Entries	Pull Mean	Pull Width
$X_{D_0^{*0}}$	300	-0.061 ± 0.060	0.975 ± 0.041
$Y_{D_0^{*0}}$	300	0.102 ± 0.058	0.964 ± 0.044
X_{NonRes}	300	-0.036 ± 0.057	0.924 ± 0.039
Y_{NonRes}	300	0.082 ± 0.056	0.907 ± 0.042
$m(D_2^{*0})$	300	0.236 ± 0.179	0.152 ± 0.238
$\Gamma(D_2^{*0})$	300	0.304 ± 0.298	0.249 ± 0.393
$m(D_0^{*0})$	300	0.302 ± 0.298	0.247 ± 0.394
$\Gamma(D_0^{*0})$	300	0.302 ± 0.298	0.247 ± 0.394

Table 10: Ensemble 4 fit validation results, with floating mass and width for both D_2^{*0} and D_0^{*0}.

Fit Parameter	Entries	True Value	Pull Mean	Pull Width
$X_{D_0^{*0}}$	300	1.0	-0.016 ± 0.063	0.970 ± 0.047
$Y_{D_0^{*0}}$	300	0.0	0.054 ± 0.066	1.017 ± 0.057
X_{NonRes}	300	0.0	-0.007 ± 0.063	0.959 ± 0.049
Y_{NonRes}	300	0.0	0.010 ± 0.058	0.932 ± 0.049
$m(D_2^{*0})$	300	2.4626	0.194 ± 0.179	0.152 ± 0.238
$\Gamma(D_2^{*0})$	300	0.049	0.263 ± 0.298	0.249 ± 0.393
$m(D_0^{*0})$	300	2.318	0.260 ± 0.298	0.247 ± 0.394
$\Gamma(D_0^{*0})$	300	0.267	0.260 ± 0.298	0.247 ± 0.394

Table 11: Ensemble 4 fit validation results but with asymmetric error calculation, rather than parabolic as in table 10 with floating mass and width for both D_2^{*0} and D_0^{*0}.

8.2.1 Results of the Ensemble Tests

Based on the results from the ensemble tests summarized in Tables 7–10, we conclude that the fit framework is unable to reliably evaluate the mass and width of both the D_0^{*0} and D_2^{*0} resonances when these parameters are allowed to float.

In Ensemble 1 (Table 7), where all resonance parameters are fixed, the pull widths for the amplitude components are close to one. This suggests that the fit framework performs well under these conditions, with uncertainties appropriately estimated and no significant biases present.

Fit Parameter	Entries	True Value	Pull Mean	Pull Width
$X_{D_0^{*0}}$	300	-0.096	-0.058 ± 0.061	0.988 ± 0.050
$Y_{D_0^{*0}}$	300	-0.271	0.006 ± 0.063	1.014 ± 0.053
X_{NonRes}	300	-0.315	-0.015 ± 0.057	0.929 ± 0.043
Y_{NonRes}	300	-0.196	0.047 ± 0.058	0.954 ± 0.047
$m(D_2^{*0})$	300	2.4626	0.236 ± 0.179	0.152 ± 0.238
$\Gamma(D_2^{*0})$	300	0.049	0.304 ± 0.298	0.249 ± 0.393
$m(D_0^{*0})$	300	2.318	0.302 ± 0.298	0.247 ± 0.394
$\Gamma(D_0^{*0})$	300	0.267	0.302 ± 0.298	0.247 ± 0.394

Table 12: Results of ensemble tests for a random model leaving all parameters of interest floating. The mass and width of $D_0^{*0}(2400)^0$ and D_0^{*02} is given in GeV/c^2.

Fit Parameter	Entries	True Value	Pull Mean	Pull Width
$X_{D_0^{*0}}$	300	-0.300	0.185 ± 0.057	0.923 ± 0.046
$Y_{D_0^{*0}}$	300	0.057	0.024 ± 0.063	0.986 ± 0.052
X_{NonRes}	300	-0.375	0.152 ± 0.060	0.978 ± 0.048
Y_{NonRes}	300	-0.049	-0.083 ± 0.063	0.983 ± 0.063
$m(D_2^{*0})$	300	2.4626	0.239 ± 0.186	0.157 ± 0.249
$\Gamma(D_2^{*0})$	300	0.049	0.309 ± 0.297	0.252 ± 0.387
$m(D_0^{*0})$	300	2.318	0.302 ± 0.298	0.247 ± 0.394
$\Gamma(D_0^{*0})$	300	0.267	0.302 ± 0.298	0.247 ± 0.394

Table 13: Results of ensemble tests for another random model leaving all parameters of interest floating. The mass and width of the D_0^{*00} and D_0^{*02} is given in GeV/c^2.

However, when the mass and width of the resonances are allowed to float, as in Ensembles 2–4, the pull widths for these parameters deviate substantially from one:

- In Ensemble 2 (Table 8), with floating D_2^{*0} mass and width, the pull widths for $m(D_2^{*0})$ and $\Gamma(D_2^{*0})$ are 0.152 ± 0.238 and 0.249 ± 0.393, respectively. These values are approximately **85% and 75% lower, respectively** than the expected value of one, indicating a significant underestimation of the uncertainties in the fit to these parameters.

- In Ensemble 3 (Table 9), with floating D_0^{*0} mass and width, the pull widths for $m(D_0^{*0})$ and $\Gamma(D_0^{*0})$ are also 0.152 ± 0.238 and 0.249 ± 0.393, respectively, mirroring the deviations observed in Ensemble 2. The same problem exists in ensemble 4 (Table 10)as well.

Pull plots for ensemble 4, showing the deviation of the pull width from 1, can be found in Appendix **??**.

These deviations indicate that the fit framework lacks the necessary sensitivity and accuracy to estimate the mass and width parameters of the resonances when they are not fixed. Therefore, to ensure the reliability of the fit results, all resonance parameters are fixed, allowing for a stable amplitude fit where the amplitude coefficients for the isobar model can be accurately determined.

However, this study underscores the need for a comprehensive investigation of the fitting framework, LAURA^{++}, to identify potential limitations and improve the accuracy of uncertainty estimation for resonance parameters when they are allowed to float.

9 Fit Result

In this section, we present the fit results for the model, including efficiency corrections and calculated weights. In accordance to the discussion in Section 8.2.1, where only the coefficients of the isobar model are allowed to float. The fits are repeated multiple times and the best value of NLL is selected, to ensure the fit does not get stuck at a local minima. However, an overestimation of the amplitude for the D_2^{*0} component is observed, as shown in Figure 20a. The fits to the Dalitz plot (DP) variables, along with the corresponding DP distribution, are shown in Figures 20 – 23.

Fit Parameter	Result	Error
$X_{D_0^{*0}}$	-0.568103	0.021627
$X_{D_2^{*0}}$	fixed	fixed
X_{NonRes}	-1.069784	0.050255
$Y_{D_0^{*0}}$	-0.40408	0.027464
$Y_{D_2^{*0}}$	fixed	fixed
Y_{NonRes}	-1.926163	0.035656
$FF_{D_0^{*0}}$	0.086894	-
$FF_{D_2^{*0}}$	0.178786	-
FF_{NonRes}	0.867923	-
$FF_{D_0^{*0},D_2^{*0}}$	-0.001914	-
$FF_{D_0^{*0},\text{NonRes}}$	-0.131583	-
$FF_{D_2^{*0},\text{NonRes}}$	-0.000105	-
$\bar{\epsilon}$	0.007752	-

Table 14: Results of the final fit on the generic MC collection of BELLE II.

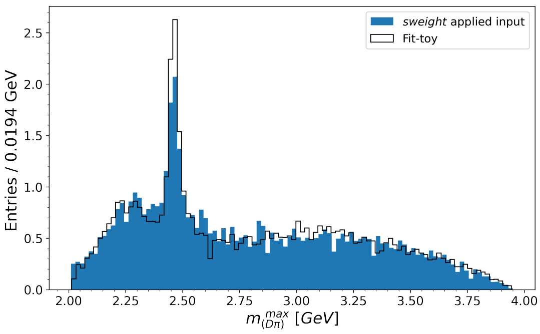

(a)

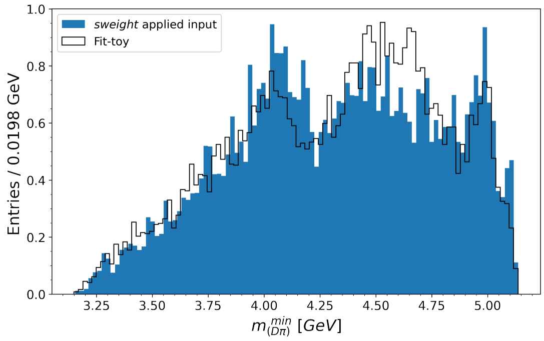

(b)

Figure 20: Fit to the Dalitz plot variable (a) $m(D\pi)_{max}$ and (b) $m(D\pi)_{min}$

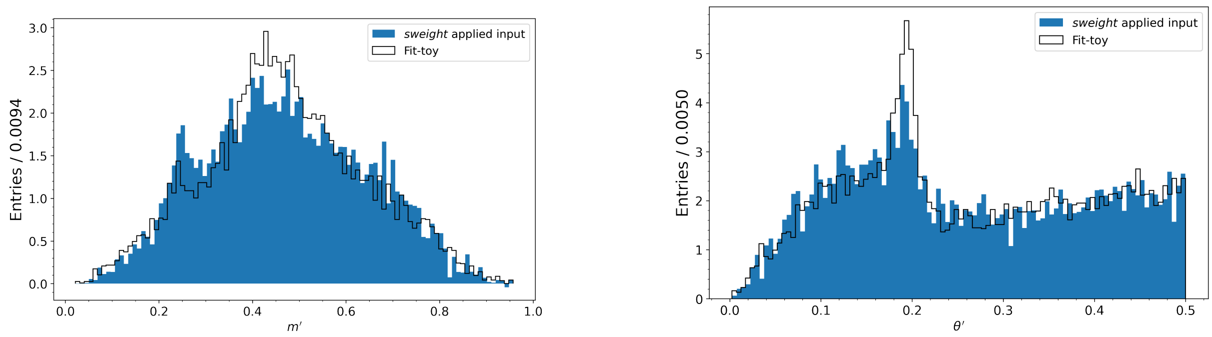

(a) (b)

Figure 21: Fit to the Dalitz plot variable (a) m' and (b) θ' respectively

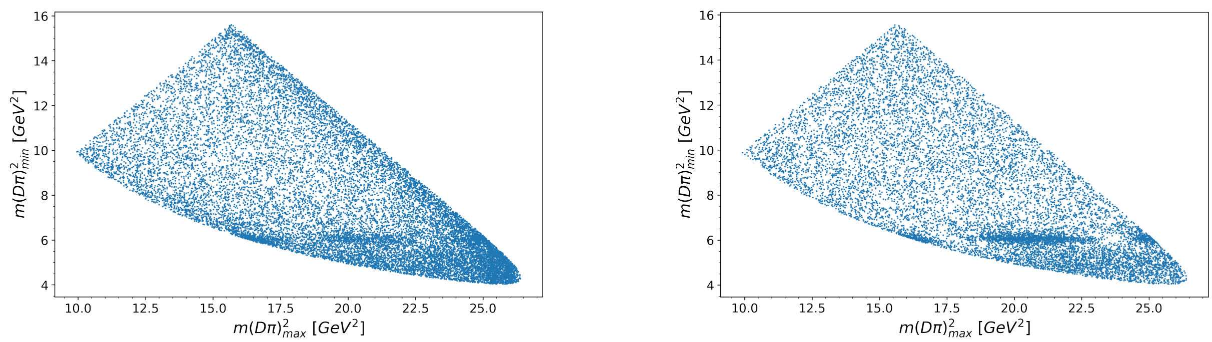

(a) (b)

Figure 22: Comparison of (a) input and the (b) fit on the Dalitz plot

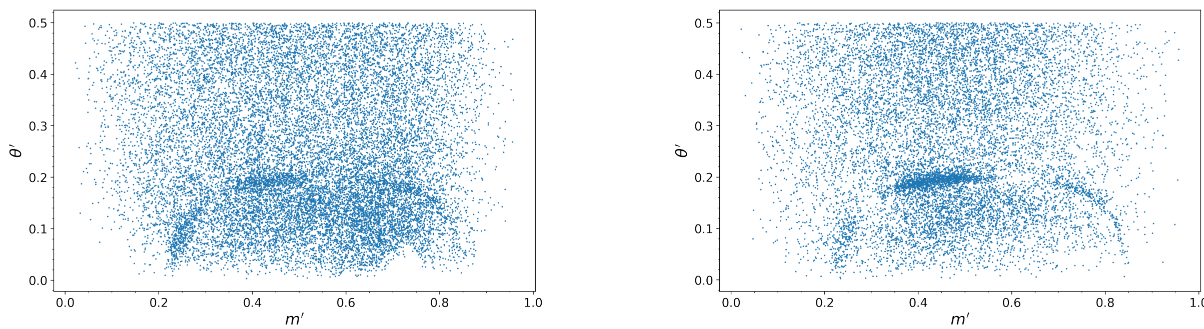

(a) (b)

Figure 23: Comparison of (a) input and the (b) fit on the Square Dalitz plot

10 Conclusion

In this thesis, a Dalitz analysis of the decay $B^- \to D^+\pi^-\pi^-$ was performed on simulated BELLE II data, corresponding to an integrated luminosity of 699.235 fb^{-1}, collected at the $\Upsilon(4S)$ resonance energy. This analysis aimed to identify the intermediate resonances within the decay and to extract various parameters of interest, such as resonance masses and widths, from a single fit. Although the primary objective was to determine these parameters with improved precision, challenges in calculating uncertainties—particularly in ensemble tests (toy studies) used to validate Dalitz fits—posed significant obstacles.

Additionally, a background subtraction technique was implemented, allowing for a simplified treatment of background contributions. This approach minimized the need for precise background modeling and reduced concerns about background efficiency, saving considerable time in the analysis process.

The observed overestimation of the amplitude indicates a need for a more accurate description of the lineshapes of the underlying components. To address this, an model independent way for the S-wave component of the $D\pi$ system was tested. While this adjustment reduced the overestimation, it could not be fully included in this analysis due to the low statistics of the D_0^{*0} component.

Looking forward, improvements in line shapes, incorporation of systematic uncertainties, and resolution of issues within the fitting framework (Laura^{++}) related to uncertainty estimation will enable a more accurate determination of resonance parameters through Dalitz analysis.

A Appendix

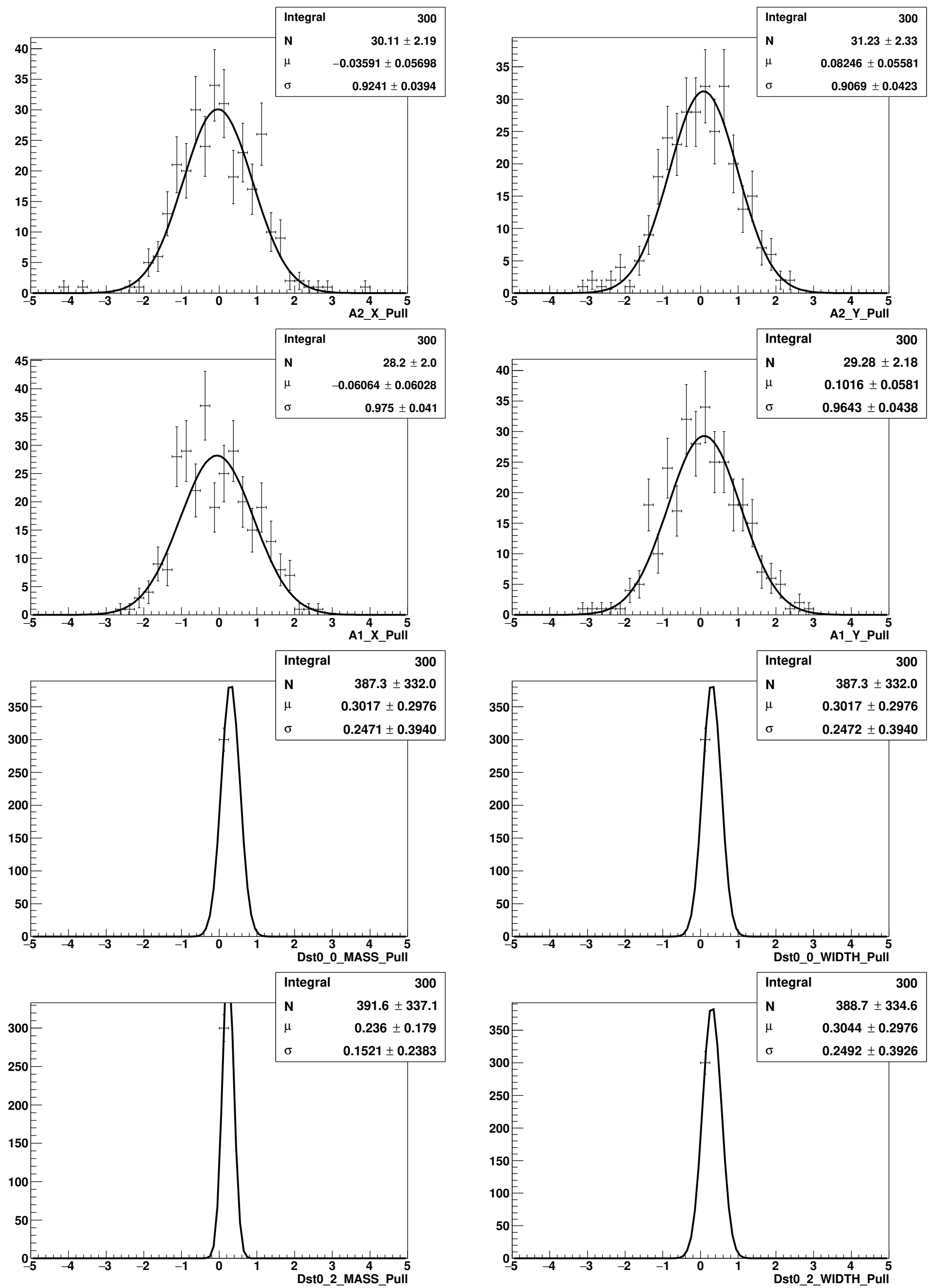

Figure 24: Pull plots for Ensemble 4.

Bibliography

[1] Kazuo Abe et al. Study of B- —> D**0 pi- (D**0 —> D(*)+ pi-) decays. *Phys. Rev. D*, 69:112002, 2004.

[2] Y. Suetsugu, H. Fukuma, K. Ohmi, M. Tobiyama, John Flanagan, H. Ikeda, Emy Mulyani, K. Shibata, T. Ishibashi, M. Shirai, Shinji Terui, Kouji Kanazawa, and H. Hisamatsu. Mitigating the electron cloud effect in the superkekb positron ring. *Physical Review Accelerators and Beams*, 22, 02 2019.

[3] Paolo Branchini. The belle ii experiment: Status and prospects. *Universe*, 4(10), 2018.

[4] A. J. Bevan, B. Golob, Th. Mannel, S. Prell, and B. D. Yabsley. The physics of the b factories. *European Physical Journal C*, 74:3026, 2014. SLAC-PUB-15968, KEK Preprint 2014-3.

[5] S. Navas and others (Particle Data Group). Review of particle physics. *Phys. Rev. D*, 110(3):030001, 2024.

[6] Giulia Ricciardi and Marcello Rotondo. Determination of the cabibbo-kobayashi-maskawa matrix element $|V_{cb}|$. *Journal of Physics G: Nuclear and Particle Physics*, June 2020.

[7] BABAR Collaboration. Dalitz plot analysis of $B^- \to D^+\pi^-\pi^-$. *Phys. Rev. D*, 79:112004, Jun 2009.

[8] R. Aaij et al. Amplitude analysis of $b^- \to d^+\pi^-\pi^-$ decays. *Physical Review D*, 94(7), 2016.

[9] Kazunori Akai, Kazuro Furukawa, and Haruyo Koiso. Superkekb collider. *Nuclear Instruments and Methods in Physics Research Section A: Accelerators, Spectrometers, Detectors and Associated Equipment*, 907:188–199, November 2018.

[10] Simon Kohl. Dalitz analysis of $B^- \to D^+\pi^-\pi^-$. Master's thesis, Karlsruhe Institute of Technology (KIT), 2016.

[11] E. Kou, P. Urquijo, and Belle II Collaboration. The belle ii physics book. *Progress of Theoretical and Experimental Physics*, 2019(12):123C01, 12 2019.

[12] T. Abe, I. Adachi, et al. Belle ii technical design report. Technical report, Belle II Collaboration, 2010. arXiv:1011.0352.

[13] V. Brancolini and L. Linssen, editors. *CERN-BINP Workshop for Young Scientists in e+e- Colliders*, volume 1 of *CERN-Proceedings*, Geneva, Switzerland, 2017.

[14] Philipp Feichtinger. *Test of light-lepton universality in tau decays with data from the Belle II experiment*. PhD thesis, Technische Universität Wien, 2024. reposiTUm.

[15] M. Mikhasenko, M. Albaladejo, Ł. Bibrzycki, C. Fernández-Ramírez, V. Mathieu, S. Mitchell, M. Pappagallo, A. Pilloni, D. Winney, T. Skwarnicki, and A.P. Szczepaniak. Dalitz-plot decomposition for three-body decays. *Physical Review D*, 101(3), February 2020.

[16] John Back, Tim Gershon, Paul Harrison, and et al. Laura^{++}: A dalitz plot fitter. *Computer Physics Communications*, 231(3):198–242, oct 2018.

[17] David J. Herndon, Paul Söding, and Roger J. Cashmore. Generalized isobar model formalism. *Phys. Rev. D*, 11:3165–3182, Jun 1975.

[18] C. Zemach. Three pion decays of unstable particles. *Phys. Rev.*, 133:B1201–B1205, 1964.

[19] C. Zemach. Use of angular-momentum tensors. *Phys. Rev.*, 140:B97–B108, 1965.

[20] J. Blatt and V. E. Weisskopf. *Theoretical Nuclear Physics*. J. Wiley, New York, 1952.

[21] Bernard Aubert et al. An amplitude analysis of the decay b± → ±±. *Phys. Rev.*, D72:052002, 2005.

[22] Volker Blobel and Erich Lohrmann. *Statistische und numerische Methoden der Datenanalyse*. Springer-Verlag, 2013.

[23] R. Brun and F. Rademakers. ROOT: An object oriented data analysis framework. *Nucl. Instrum. Meth. A*, 389:81–86, 1997.

[24] F. James and M. Roos. Minuit - a system for function minimization and analysis of the parameter errors and correlations. *Computer Physics Communications*, 10(6):343–367, 1975.

[25] Yuehong Xie. sfit: a method for background subtraction in maximum likelihood fit, 2009.

[26] M. Pivk and F.R. Le Diberder. : A statistical tool to unfold data distributions. *Nuclear Instruments and Methods in Physics Research Section A: Accelerators, Spectrometers, Detectors and Associated Equipment*, 555(1–2):356–369, December 2005.

[27] Phillip Urquijo and Torben Ferber. Overview of the belle ii physics generators. Technical Report BELLE2-NOTE-PH-2015-006, School of Physics, The University of Melbourne, Victoria 3010 and University of British Columbia, Vancouver, BC, Canada V6T 1Z1, March 2016.

[28] S. Jadach, B.F.L. Ward, Z. Was, S.A. Yost, and A. Siodmok. Multi-photon monte carlo event generator kkmcee for lepton and quark pair production in lepton colliders. *Computer Physics Communications*, 283:108556, 2023.

[29] Christian Bierlich, Smita Chakraborty, Nishita Desai, Leif Gellersen, Ilkka Helenius, Philip Ilten, Leif Lönnblad, Stephen Mrenna, Stefan Prestel, Christian T. Preuss, Torbjörn Sjöstrand, Peter Skands, Marius Utheim, and Rob Verheyen. A comprehensive guide to the physics and usage of PYTHIA 8.3. *SciPost Phys. Codebases*, page 8, 2022.

[30] Christian Bierlich, Smita Chakraborty, Nishita Desai, Leif Gellersen, Ilkka Helenius, Philip Ilten, Leif Lönnblad, Stephen Mrenna, Stefan Prestel, Christian T. Preuss, Torbjörn Sjöstrand, Peter Skands, Marius Utheim, and Rob Verheyen. Codebase release 8.3 for PYTHIA. *SciPost Phys. Codebases*, pages 8–r8.3, 2022.

[31] David J. Lange. The evtgen particle decay simulation package. *Nuclear Instruments and Methods in Physics Research Section A: Accelerators, Spectrometers, Detectors and Associated Equipment*, 462(1):152–155, 2001. BEAUTY2000, Proceedings of the 7th Int. Conf. on B-Physics at Hadron Machines.

[32] N. Davidson, T. Przedzinski, and Z. Was. Photos interface in c++; technical and physics documentation, 2015.

[33] S. Agostinelli, J. Allison, K. Amako, and et al. Geant4—a simulation toolkit. *Nuclear Instruments and Methods in Physics Research Section A: Accelerators, Spectrometers, Detectors and Associated Equipment*, 506(3):250–303, 2003.

[34] Thomas Kuhr, Christian Pulvermacher, Martin Ritter, et al. The belle ii core software. *Computing and Software for Big Science*, 3(1):1, 2019.

[35] T. Keck, F. Abudinén, et al. The full event interpretation. *Computing and Software for Big Science*, 3(1):6, Feb 2019.

[36] Manuel Heider. *Dalitz analysis of $B^- \to D^0\pi^-\pi^0$ and $B^0 \to D^-\pi^+\pi^0$ at the Belle experiment.* PhD thesis, KIT, Karlsruhe, 2015.

[37] J.-F. Krohn, F. Tenchini, P. Urquijo, and et al. Global decay chain vertex fitting at Belle II. *Nuclear Instruments and Methods in Physics Research Section A: Accelerators, Spectrometers, Detectors and Associated Equipment*, 976:164269, 2020.

[38] M. G. Kendall. A new measure of rank correlation. *Biometrika*, 30(1/2):81–93, 1938.